Journal Pre-proofs

HBIM symmetry parametrization using TLS and UAV LiDAR measurements

Pawel S. Dabrowski, Marek H. Zienkiewicz, Paweł Tysiąc, Paweł Burdziakowski, Jakub Szulwic, Jūratė Sužiedelytė-Visockienė, Eimuntas Paršeliūnas, Romuald Obuchovski, Rokas Bražiūnas, Rafał Ossowski

PII: S0263-2241(25)01109-1
DOI: https://doi.org/10.1016/j.measurement.2025.117750
Reference: MEASUR 117750

To appear in: *Measurement*

Received Date: 27 February 2025
Revised Date: 23 April 2025
Accepted Date: 30 April 2025

Please cite this article as: P.S. Dabrowski, M.H. Zienkiewicz, P. Tysiąc, P. Burdziakowski, J. Szulwic, J. Sužiedelytė-Visockienė, E. Paršeliūnas, R. Obuchovski, R. Bražiūnas, R. Ossowski, HBIM symmetry parametrization using TLS and UAV LiDAR measurements, *Measurement* (2025), doi: https://doi.org/10.1016/j.measurement.2025.117750

Title:

HBIM symmetry parametrization using TLS and UAV LiDAR measurements

Author Information

Author names:

Pawel S. Dabrowski [1,*], Marek H. Zienkiewicz [1], Paweł Tysiąc [1], Paweł Burdziakowski [1], Jakub Szulwic [1], Jūratė Sužiedelytė-Visockienė [2], Eimuntas Paršeliūnas [2], Romuald Obuchovski [2], Rokas Bražiūnas [2], Rafał Ossowski [1]

Affiliations:

1 - Faculty of Civil and Environmental Engineering, Gdańsk University of Technology, Gabriela Narutowicza 11/12, 80-233 Gdańsk, Poland

2 - Faculty of Environmental Engineering, Vilnius Gediminas Technical University, Saulėtekio Av, 11, LT-10223 Vilnius, Lithuania

Corresponding author:

* - Corresponding author: Pawel S. Dabrowski, e-mail: pawel.s.dabrowski@pg.edu.pl

Abstract

The paper describes a new approach to the assessment of symmetry in HBIM datasets on the example of the Tower of Gediminas in Vilnius (Lithuania). Symmetry is a principal component of the design and construction of ancient, medieval, Renaissance, and other epochs. The unified methodology involves the processing of LiDAR point clouds and applies to objects with a regular polygon cross-section. Proposed HBIM parameters introduce a uniform description of features of symmetry of historical buildings, which provides new insights into the original design of spatial relationships between the buildings' architectural elements useful for professional conservators and renovators. The validation of the new approach involved well-established TLS and, taking into account the current development of drone technologies, ALS measurements. The obtained converging and similar estimates showed the applicability of both LiDAR technologies. Hence, the study proposes the introduction of the new symmetry parameters into the HBIM products and software.

Keywords: HBIM; symmetry; deformations; historical buildings; PCSE

1 Introduction

Historic building information modeling (HBIM) is a system proposed in 2009 for collecting, storing, modeling and interpreting data on European historic structures, while the related term of heritage building information model describes the final result of the modeling process **[1-4]**. Initially, the authors of the concept envisaged the use of point clouds from terrestrial laser scanning (TLS) and close-range photogrammetry in the inventory of the shape of objects **[5-6]**. However, the development of the field of airborne drones (UAV) has significantly broadened the spectrum of applications of high-resolution optical and multispectral cameras and LiDAR (Light Detection and

Ranging) sensors in documenting cultural heritage **[7-9]**. Standard areas of application for ALS LIDAR include environmental topographic analyses **[10-11]** and forestry **[12]**. Currently, one of the main directions of HBIM development is the implementation of artificial intelligence and deep learning in the analysis and interpretation of source object models (point clouds or images) **[13-14]**.

The creators of the HBIM term proposed to extend the building information model (BIM) that has been used since the 1970s with additional geometric and descriptive parameters typical of historic buildings **[15]**. The standardization of the BIM term occurred through the introduction in 2013 and two revisions of the ISO 16739 standard **[16]**. Additionally, the process of creating and maintaining BIM systems is the subject of a separate ISO 19650 standard **[17]**. The extension of the existing BIM model to HBIM consisted of the creation of a geometric descriptive language (GDL) to build complex parametric objects and the development of a library of parameters based on historical data described in the archival sources **[18]**. An additional practical aspect of the system is the creation of software that combines source data from the measurement and the HBIM library **[1-2]**. In general, it can be assumed that BIM focuses on designed and newly constructed facilities, while HBIM is dedicated to existing historical buildings and serves to document and recreate their lifespan **[19]**.

HBIM, apart from the geometric aspect, includes metadata about the history, materials, and deterioration processes of historical buildings **[20]**. Semantic segmentation methods **[21]**, semi-automatic modeling of building facades **[22]**, and Level of Detail (LoD) structure decomposition **[23]** are important enrichments of HBIM datasets. Additionally, the development of HBIM consisted of taking into account factors of diagnostics and detection of structural damage and then proposing means of conservation and renovation of historical buildings **[24]**. The above factors constitute a reliable basis for decision-making regarding the maintenance of historical buildings **[25]**, which was presented in practical examples of HBIM implementation in documentation and facility management **[26-27]**. The literature emphasizes the significant importance of point cloud registration and the integration of point clouds captured by different sensors **[28]**. The first of these topics is extensively discussed in publications describing point cloud registration methods. The second concerns the challenge of harmonizing the coordinate systems of two datasets **[29-30]**. Our approach incorporates an additional factor in the determination of transformation parameters, the cardinal orientation, which considers the object's position relative to geographic directions.

The conducted literature analysis showed that the set of HBIM parameters does not include the symmetry factor of historical buildings **[19, 31-34]**. The standard approach used in HBIM works is the modeling of geometric features based on point clouds obtained from terrestrial or airborne scanning. Additionally, supplementary visual inspections and in-situ measurements are sometimes performed **[35]**, as well as the use of active and passive tools **[36]**. Symmetry, a fundamental concept in geometry, can provide valuable insights into the design intent, construction techniques, and potential structural defects. Bilateral, radial, and translational symmetry was a crucial architectural principle in ancient, medieval, and Renaissance epochs **[37-39]**. The HBIM aims are documentation, preservation, and restoration of historical structures, hence the symmetry-oriented evaluation in HBIM applications was conducted in several case studies **[40-42]**. However, no universal solution for the symmetry parametrization has been proposed yet to help cultural heritage conservators to understand the original design of spatial relationships between the buildings' architectural elements.

Symmetry parameterization, in the case of point cloud data, involves the development of a mathematical algorithm to identify and quantify the geometric relationships between corresponding points or features on the object and its axis of symmetry. The limitation of the LiDAR data acquisition, especially of airborne laser scanners (ALS) mounted on an airborne drone but also the terrestrial laser scanners (TLS), is a significant difficulty or, in some cases, impossibility to measuring in narrow corridors and stairs of eg. medieval towers. Hence, the gathered data contain a digital representation of the accessible surface, which is used in the detailed description of the general shape and irregularities of the exterior of the historical buildings. The novelty of the study is presenting a unified methodology for assessing the symmetry of regular polygon historical buildings to implement in HBIM datasets. The new HBIM symmetry parameters include:

- multi-modal course of the symmetry axis describing the arrangement of successive storeys of the building,
- spatial orientation and inclination of wall panels in relation to the designated axis of symmetry of the building,
- regularity of the position of vertical wall edges related to the theoretical geometry of the structure.

The presented set of parameters defines the actual shape of a symmetrical historical structure in relation to the theoretical shape of the original solid, which may be, for example, a cylinder or a regular prism. The presented parameters introduce a detailed descriptive attributes defining the feature of symmetry of historical buildings to be introduced in the HBIM softwares. Such information would be valuable for historians, architects, conservators and renovators of cultural heritage objects.

Taking into account the exceptional cases of availability of design or technical archival documentation of the analyzed historical buildings, the research methodology includes the scenario of the lack of archival data and an estimation of the shape of the primary primitive (solid) based on the measurement results. Taking the obtained solid as a reference value, the topological dependencies of the points from the cloud and the walls of the solid are determined as a depth parameter used in the point cloud spatial expansion (PCSE) method **[43-44]**. An important element of the PCSE method is the procedure of estimating the axis of a symmetrical object, in relation to which all HBIM symmetry features of the historical building are determined **[45]**.

The test object of the study is The Gediminas Castle Tower in Vilnius, the capital of Lithuania. This Gothic castle is the only surviving fortification tower of the Upper Castle, which was partially destroyed during World War II. After the war, the tower was reconstructed and currently, it is the most visited facility of the National Museum of Lithuania. The steep slopes of Castle Hill involve landslide hazards, which have been the subject of several geological studies involving potential displacements and deformations of the tower **[46-48]**. The application and validation of the developed HBIM symmetry methodology were carried out on point clouds from two independent sensors: a terrestrial laser scanner (TLS) and an airborne laser scanner (ALS) mounted on an airborne drone. Hence, the secondary aim of the study was to verify and quantify new HBIM features calculated in two source datasets. The experiment verified positively the hypothesis about similar accuracy and converging values of HBIM parameters of symmetry obtained from the data from the UAV and TLS point clouds. The proposed solution is a innovative and unified approach for the assessment of geometry that is applicable generally for symmetrical historical buildings. It can also be used in periodic monitoring and regular object maintenance. The analysis algorithm was implemented in the authors' software written in Python. Data visualization and control of the integration of TLS and ALS point clouds were carried out in CloudCompare **[49]**.

2 Material and methods

The section is divided into three subsections. The first **Subsection 2.1** describes the measurements and registration of the analyzed point clouds of the Tower of Gediminas. It presents the measuring sensors and the conditions for using TLS and UAV LiDAR technologies. The second **Subsection 2.2** describes the pre-processing of the point clouds for further estimating the symmetry parameters of symmetrical historical objects. The third **Subsection 2.3** is the major part of the study and presents algorithms for determining the angular, linear, and surface symmetry parameters to be included in the HBIM datasets. The study's workflow is presented in **Fig. 1**.

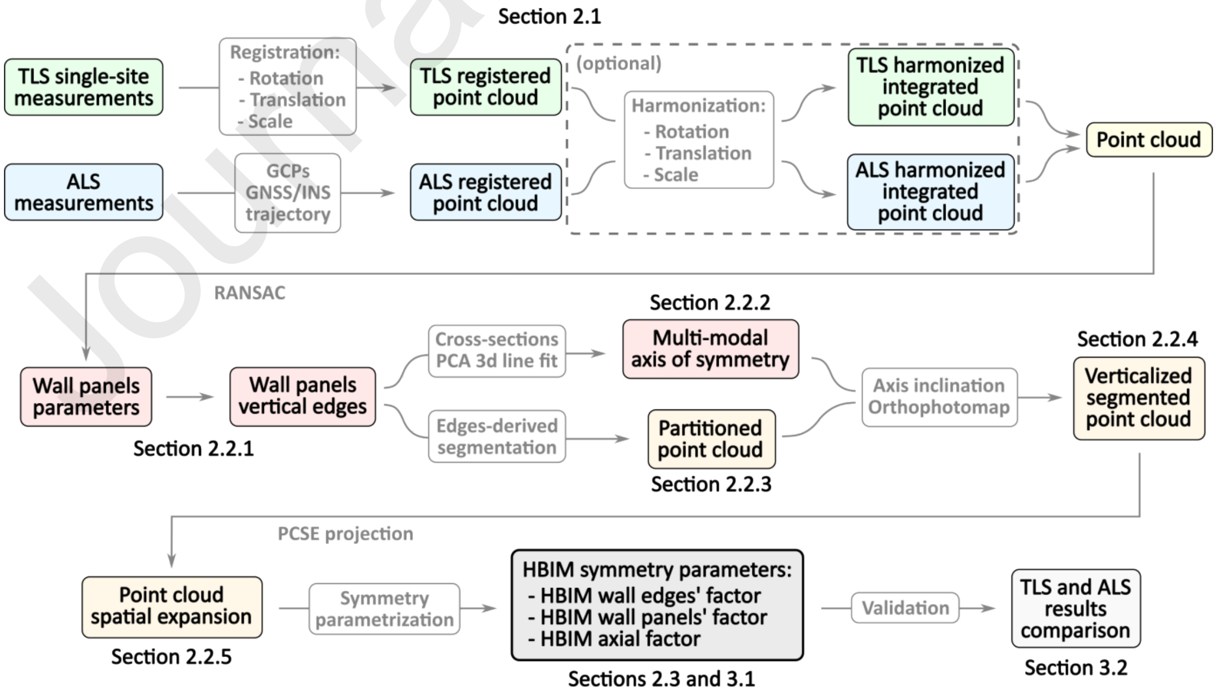

Fig. 1. The algorithm of determination and validation of the HBIM symmetry parameters.

2.1 Measurements and point cloud registration

2.1.1 Ground control points

Establishing Ground Control Points (GCPs) is fundamental to ensuring high-fidelity integration of Terrestrial Laser Scanning (TLS) and UAV-based laser scanning (ALS) datasets, especially when seeking sub-centimeter to centimeter-level precision suitable for heritage documentation and HBIM applications **[50-51]**. GCPs serve as physical markers with known coordinates in a global or local coordinate system (e.g., EPSG codes), so that each independent dataset (TLS or UAV) can be accurately tied to the same spatial reference **[52]**. The following paragraphs describe the approach adopted in this study and highlight both best practices and precision considerations drawn from geomatics research. The Tower of Gediminas measurements and location are presented in **Fig. 2**.

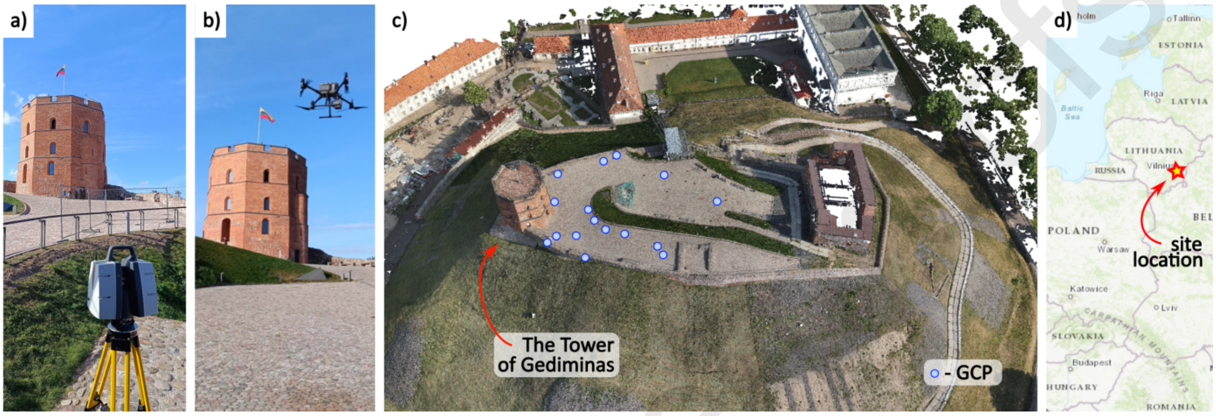

Fig. 2. TLS (a) and UAV (b) LiDAR measurements with the locations of the GCPs (c) and the research site (d).

Prior to data collection, the complex geometry of the Gediminas Tower and its surrounding terrain was analyzed to identify optimal placements for GCPs. The presence of steep slopes, retaining walls, and visitor pathways required careful planning to ensure line-of-sight between the GCPs and both the terrestrial scanner and UAV flight paths **[53]**. Eleven GCPs were placed around the tower's perimeter, favoring unobstructed locations and areas likely to be visible from multiple scan positions. A higher density of GCPs was used near corners and recessed portions to mitigate occlusion effects that are common in medieval or irregularly shaped buildings. This approach aligns with typical practice in geomatics, where at least five to ten GCPs are recommended for small-to-medium scale heritage sites, depending on site complexity and required accuracy.

A high-precision GNSS receiver (e.g., JAVAD Triumph-2) was used in RTK mode with corrections from the LitPOS network (average baseline ~5 km). Short baselines are beneficial for reducing ionospheric and tropospheric errors. Each GCP was occupied for at least 3 minutes to achieve stable solutions, resulting in a typical horizontal precision of 10–15 mm and vertical precision of ~20 mm. Repeated measurements were performed on each GCP to confirm reliability. Discrepancies greater than 20–30 mm triggered reoccupation or extension of observation time until consistency was achieved. This helped ensure that the GCP network introduced minimal error when aligning the TLS and UAV datasets.

During post-processing, GCP coordinates were employed to transform the TLS and UAV LiDAR point clouds into the same coordinate system (EPSG: 3346). These GCPs acted as "anchor points," so that any residual misalignment or drift (particularly in the UAV flight trajectory) was minimized **[54]**. Using GCPs, we verified the overall registration accuracy of the combined point cloud by evaluating differences between GCP coordinates observed in TLS or UAV data versus their known GNSS-based coordinates. For each GCP, this difference was generally below 20–30 mm, matching expectations for combining datasets of different vantage points in a complex urban/heritage environment. By adhering to the above workflow and leveraging robust GCP placement, the final transformation of both TLS and UAV LiDAR data into one unified reference frame achieved sub-3 cm alignment accuracy around the tower. This level of precision is typically acceptable for geometrical analyses in HBIM, such as wall deflection or structural monitoring, where large-scale deformation tracking or symmetry assessments are of interest **[14].**

2.1.2 TLS and ALS point clouds

Accurate, high-density 3D point clouds of the Tower of Gediminas were acquired with two complementary platforms: (1) a Terrestrial Laser Scanner (TLS), offering millimeter to sub-centimeter resolution in near-field areas; and (2) a UAV-mounted LiDAR system (ALS), providing coverage of upper portions of the tower, difficult to capture from the ground. Although each approach has distinct advantages, the integration requires careful attention to resolution, scanning geometry, and final registration results **[55].** Medieval towers, especially those situated on steep slopes like the Gediminas Hill, pose significant challenges for ground-based surveys. High walls, protruding architectural elements, and restricted access around the site can create blind spots in TLS scans. While multiple TLS stations can reduce occlusions, each additional scan position increases survey time and registration complexity **[51]**. UAV LiDAR alleviates many of these issues by capturing overhead perspectives. Even if the data from the UAV sensor are sparser, these aerial vantage points ensure the roof and upper facades are accurately mapped. This synergy between high-density TLS coverage at lower levels and aerial scanning at upper levels yields a more complete dataset with fewer voids or "shadow zones."

The Tower of Gediminas features irregular masonry, steep vertical offsets, and historically modified upper segments—all of which require consistent spatial coverage. TLS excels at capturing fine details at short-to-medium ranges, achieving point densities of a few millimeters **[56]**. However, to reach upper segments from ground stations, incident angles worsen, and data gaps appear within recesses. By contrast, UAV LiDAR—though often criticized for producing more dispersed point clouds—can still achieve point densities of 100–400 pts/m² at lower altitudes and moderate flight speeds **[57]**. In this project, flying at approximately 40 m above ground level with slow flight trajectories, the CHC AlphaAir 450 sensor provided ~400 pts/m² at the tower's roofline—sufficient for modeling general geometry and capturing moderate architectural details. One core aim of this study is to introduce a new symmetry-related parameter set within an HBIM environment. Evaluating structural or design symmetries—such as tower verticality and wall tilt—demands reliable 3D geometry across the full height. A purely terrestrial approach would risk incomplete coverage of upper stories or roofs, while a purely aerial solution might lack the sub-centimeter precision needed at ground or mid-height levels. Hence, the dual approach provides a balance of detail and coverage that aligns with the resolution and accuracy needs of symmetry-driven HBIM analysis.

We used a Leica P30 (Manufacturer: Leica Geosystems AG - Part of Hexagon), known for its high ranging accuracy (up to ±3 mm at 50 m range) and ability to capture dense point clouds of up to several million points per scan.. The P30 also includes an integrated camera, aiding color-texture mapping for the HBIM pipeline if required.

Each TLS station targeted the tower's base and mid-level surfaces from slightly different horizontal angles to minimize occlusions. The steep slopes of Gediminas Hill required careful station leveling and stable tripods, validated by short leveling cycles. TLS stations were established around the base of the tower and near its accessible perimeter at varying distances (5–30 m) to capture both global geometry and detailed architectural elements (corners, niches, vault intrados). Occlusions were minimized by using a multi-station approach, each overlapping adjacent scans by ~30%. This ensures robust registration between scans, later refined by ICP (Iterative Closest Point) **[50].** After merging all stations, the TLS dataset reached an average point spacing of ~5–10 mm on the tower façade at lower levels, which is well-suited for detailed symmetry checks and facade-based crack or tilt analyses. Registration of TLS stations (using plane-based or target-based alignments) typically resulted in a root mean square (RMS) residual of 2–4 mm for tie objects (checkerboard targets, plane patches), as validated via references **[51, 56, 58]**.

A DJI Matrice 300 RTK equipped with an AlphaAir 450 (Manufacturer: CHCNAV, China) LiDAR sensor was employed to capture upper sections of the tower. While some consider ALS from small UAVs suboptimal for highly detailed architectural features due to potentially sparse data **[57, 59]**, several recent studies have shown that multi-return LiDAR sensors, flown at low altitude and slow speed, can yield sufficiently dense point clouds for structural analyses in HBIM **[60-61]**. In our case, typical flight altitude was ~40 m AGL, with speeds of 3–5 m/s to balance coverage and point density. Despite UAV LiDAR often resulting in lower density (e.g., 50–200 points/m²) compared to TLS (up to thousands of points/m²), the AlphaAir 450 sensor provided an average of ~400 points/m² around the tower's upper walls. This density, while lower than terrestrial scans near ground level, was enough to model parapets, crenellations, and the rooftop structure with ~2–3 cm sampling intervals. Flight was planned around the tower's summit to maximize overlap. GNSS–INS (Inertial Navigation System) data were processed with RTK corrections from a nearby base station (~5 km away), yielding a horizontal accuracy of ~1–2 cm and vertical accuracy of ~2–3 cm around the tower's roof **[62]**.

With each dataset placed in the same georeferenced coordinate system (Section 2.1.1), both the TLS and UAV point clouds were imported into a common processing environment (e.g., Riscan PRO (Manufacturer: Riegl GmbH.). The integration workflow comprises four primary stages: (1) Coarse Registration, (2) Establishment of a Common Coordinate Frame, (3) ICP-Based Refinement, and (4) Generation of the Resulting Hybrid Model.

Each stage is discussed below with emphasis on methodology, achieved precision, and the practical advantages and limitations inherent to the hybrid approach.

1. Coarse Registration

TLS Scans: Each TLS station was independently registered in a common local coordinate system by employing plane-based targets. The registration process yielded root mean square (RMS) residuals in the range of 3–5 mm, which is indicative of the inherent high precision of the TLS system. This initial alignment establishes a robust foundation for integrating multiple scan positions.

UAV LiDAR: For the UAV-derived data, the flight trajectory was first refined using integrated GNSS–INS solutions. This trajectory refinement was then cross-validated against Ground Control Points (GCPs) strategically placed near the tower's upper terraces. The UAV data achieved an absolute positional accuracy within ±2–3 cm, despite the typically lower point density associated with airborne measurements.

2. Establishment of a Common Coordinate Frame

GCP-Based Alignment: To ensure both datasets could be merged accurately, GCPs were identified in the TLS scans—using checkerboard targets placed at ground level—and in the UAV LiDAR data, where reflective markers were deployed on accessible roof edges. These markers enabled a transformation of both datasets into a unified coordinate system, ensuring spatial consistency across the full height of the structure.

Coarse Merging: Following the GCP-based alignment, the TLS and UAV datasets were coarsely merged based on the known GCP coordinates. In overlapping façade areas, typical offsets were kept under 5 cm. This preliminary merging step serves as an essential precursor to further refinement, reducing large-scale misalignments before more computationally intensive processes are applied.

3. ICP Refinement

Overlap Selection: The mid-height segments of the tower—areas visible in both the TLS and UAV datasets—were selected as tie regions for the Iterative Closest Point (ICP) algorithm. Large planar surfaces, such as façade panels, were utilized as robust tie features because they are less susceptible to noise and partial occlusions, thus providing reliable correspondence between the datasets **[63-65]**.

Convergence and Accuracy: After 2–4 iterations of the ICP algorithm, the RMS differences in overlapping regions improved markedly, achieving values in the range of ~1–2 cm. Subsequent GCP cross-checks confirmed that the vertical alignment remained within 2–3 cm at the tower's parapet level. Despite occasional higher noise levels in the UAV data, the ICP refinement effectively reduced residual misalignments, thereby ensuring a high-quality unified model.

4. Resulting Hybrid Model

Density Variation: The final hybrid dataset exhibits spatial heterogeneity in point density. The lower façade, predominantly derived from TLS, benefits from sub-centimeter point spacing, while the upper surfaces—primarily captured by UAV LiDAR—show a spacing of approximately 2–3 cm. The last step was to unified method using octree to the cubic value of 10 mm for the whole tower **[66-67]**.

Although UAV LiDAR is sometimes considered too sparse for capturing the intricate details of heritage sites, careful flight planning combined with modern multi-return sensors can produce point densities sufficient for structural analyses. Increasing the number of passes and flying at slower speeds can further enhance point density, although this may compromise overall accuracy. Additionally, materials typical of historical buildings—such as brick, masonry, and uneven surfaces—often exhibit variable reflectance, which TLS generally handles well. In contrast, UAV LiDAR can generate small-scale speckle noise, particularly at steep angles. For these reasons, we restricted the use of UAV LiDAR data to the upper parts of the tower, where aerial coverage is most beneficial and the impact of speckle noise is minimized.

2.2 Data pre-processing methodology

2.2.1 Segments' axes parametrization

A point cloud is a discrete high-resolution representation of the geometry of a spatial object. Access conditions determine the completeness of the measurement of the entire object. Surrounding obstacles cause the occurrence of occlusions or non-uniform resolution of point clouds. This factor applies especially to the TLS measurements, although it is in some cases a significant obstacle in the UAV measurements. The parameterization of the shape of symmetrical objects includes the estimation of geometric primitives of planes and lines.

Noise in point clouds and the presence of architectural elements related to walls justify the application of the RANSAC filtering method **[68]** or robust M-estimation **[69]**. Resulting primitives define the basic geometric shape of the analyzed object neglecting the non-wall components of the structure. RANSAC-derived wall panels are given by plane equations:

$$A_j^i x + B_j^i y + C_j^i z + D_j^i = 0. \tag{1}$$

where *A, B, C, D* denote the coefficients of the canonical equation of the *j*-th wall plane at the *i*-th segment of the symmetric object with the normal vector of the plane $\boldsymbol{N}_j^i = \left[A_j^i, B_j^i, C_j^i\right]^T$. The result of RANSAC estimation in the TLS point cloud at the first segment of the tower is presented in **Fig. 3**.

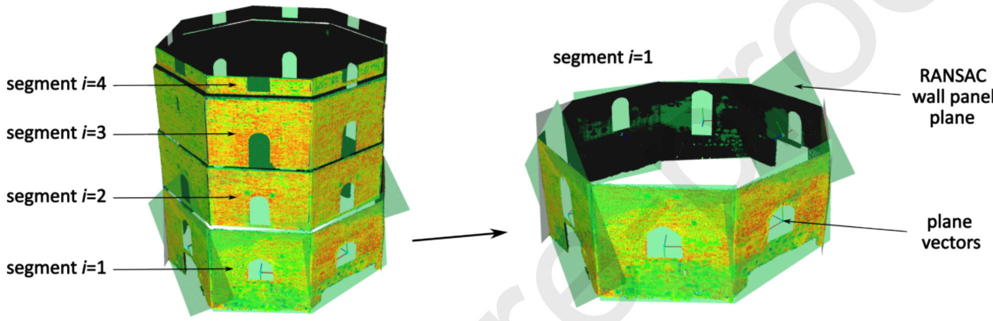

Fig. 3. RANSAC-derived wall panels' planes at segment #1 of the Tower of the Gediminas.

The next stage of calculations is the determination of the edges of the tower walls based on the intersections of the neighboring wall planes. The line in the three-dimensional Euclidean space defined by a point $\boldsymbol{P}^i_{j,mod(j+1,N)}$ and a direction vector $\boldsymbol{V}^i_{j,mod(j+1,N)}$ is determined from the equations:

$$\boldsymbol{P}^i_{j,mod(j+1,N)} = \begin{bmatrix} \frac{B_j^i D^i_{mod(j+1,N)} - B^i_{mod(j+1,N)} D^i_j}{B^i_{mod(j+1,N)} A^i_j - B^i_j A^i_{mod(j+1,N)}} & \frac{A^i_{mod(j+1,N)} D^i_j - A^i_j D^i_{mod(j+1,N)}}{A^i_j B^i_{mod(j+1,N)} - A^i_{mod(j+1,N)} B^i_j} & 0 \end{bmatrix}^T \tag{2}$$

$$\boldsymbol{V}^i_{j,mod(j+1,N)} = \begin{bmatrix} \frac{B_j^i C^i_{mod(j+1,N)} - B^i_{mod(j+1,N)} C^i_j}{B^i_{mod(j+1,N)} A^i_j - B^i_j A^i_{mod(j+1,N)}} & \frac{A^i_{mod(j+1,N)} C^i_j - A^i_j C^i_{mod(j+1,N)}}{A^i_j B^i_{mod(j+1,N)} - A^i_{mod(j+1,N)} B^i_j} & 1 \end{bmatrix}^T \tag{3}$$

where *j* and *mod*(*j*+1, *N*) denote the indices of two adjacent wall planes at the *i*-th level of the symmetrical object, *mod* denotes the modulo function with the *N*=8 representing the number of sides of the regular polygon of the tower, eg. $\boldsymbol{P}^2_{8,1}$ and $\boldsymbol{V}^2_{8,1}$ denote the point and the vector of the edge (line) between the 8-th and the 1-st wall panel on the 2-nd segment of the tower.

The axis of the symmetric object can be determined using the planes of the tower walls or the cross-sections of the point cloud. In the first case, the determination of the axis estimators involves the calculation of vertical wall edges. The vertices of eight wall edges are determined for multiple height coordinates z_{sect} for each tower segment:

$$\boldsymbol{W}^{i,z_{sect}}_{j,mod(j+1,N)} = \boldsymbol{P}^i_{j,mod(j+1,N)} + \left(\frac{z_{sect} - z_{\boldsymbol{P}^i_{j,mod(j+1,N)}}}{z_{\boldsymbol{V}^i_{j,mod(j+1,N)}}}\right) \boldsymbol{V}^i_{j,mod(j+1,N)}. \tag{4}$$

Given a set of polygon vertices $\boldsymbol{W}^{i,z_{sect}}_{j,mod(j+1,N)}$, the section's local discrete estimator of the axis $\boldsymbol{C}^{i,z_{sect}}$ is calculated:

$$C^{i,z_{sect}} = \frac{1}{6A_{sect}^{i}}\begin{bmatrix}\sum_{k=1}^{j}(x_k + x_{mod(k+1,N)})(x_k y_{mod(k+1,N)} - x_{mod(k+1,N)} y_k)\\ \sum_{k=1}^{j}(y_k + y_{mod(k+1,N)})(x_k y_{mod(k+1,N)} - x_{mod(k+1,N)} y_k)\end{bmatrix}, \tag{5}$$

where $A_{sect}^{i} = \frac{1}{2}\sum_{k=1}^{j} x_k(y_{mod(k+1,N)} - y_{mod(k-1,N)})$.

Applying the procedure for selected coordinates z_{sect} results in sets approximating the course of the axis. The independence of the axes on the four segments of the tower is assumed. Then, using the PCA method **[54]** the geometric parameters of the axis (points $\boldsymbol{P}_{axis}^{i}$ and vectors $\boldsymbol{V}_{axis}^{i}$) and the RMS of fitting points in the three-dimensional Euclidean space (RMS_{axis}^{i}) are calculated. A similar approach to determining local axis estimators uses point cloud cross-sections (cf. **[45]**). However, the applicability of cross-sections is conditioned by the point coverage of all sides of the building, and, in some cases, point cloud occlusions cause incomplete section extractions. Additionally, the axis determination by the cross-section approach is sensitive to local wall deformations which results in erroneous estimates of the axis.

A new approach involves the fitted wall planes, minimizes the limitations of the point cloud section generation, and is superior to the former cross-section approach. Each cross-section consists of points measured on eight walls of the tower. The section-based procedure begins with the LS estimatio of lines in the two-dimensional Euclidean space. As a result, the slope coefficients $a_j^{i,z_{sect}}$ and the y-intercepts $b_j^{i,z_{sect}}$ of eight fitted lines of the j-th wall, the i-th segment of the tower, and on the z_{sect} height of cross-sections are obtained. The sample estimation result is presented in **Fig. 4**.

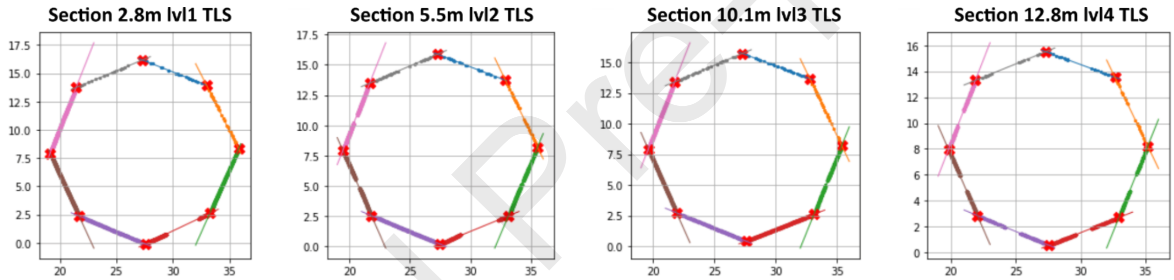

Fig. 4. Sample results of the sections' lines estimation.

The cross-section vertices of the tower point cloud $\boldsymbol{W'}_{j,j+1}^{i,z_{sect}}$ presented by red crosses in **Fig. 4** are calculated using the equation:

$$\boldsymbol{W'}_{j,j+1}^{i,z_{sect}} = -(\boldsymbol{A}^T\boldsymbol{A})^{-1}(\boldsymbol{A}^T\boldsymbol{L}), \tag{6}$$

where $\boldsymbol{A} = \begin{bmatrix} a_j^{i,z_{sect}} & -1\\ a_{mod(j+1,N)}^{i,z_{sect}} & -1\end{bmatrix}$, $\boldsymbol{L} = \begin{bmatrix} b_j^{i,z_{sect}}\\ b_{mod(j+1,N)}^{i,z_{sect}}\end{bmatrix}$.

The central points of the section ($\boldsymbol{C'}^{i,z_{sect}}$) are determined similarly to the planes-based approach using the (**Eq. 5**). The course of the symmetry axis of four tower segments can be determined using eg. Total Least Squares **[70]** or PCA (used in this study). Vector parameterization of the four segments' symmetry axes includes points $\boldsymbol{P}_{axis}^{i}$ and vectors $\boldsymbol{V}_{axis}^{i}$. The adopted fitting accuracy indicator is RMS.

2.2.2 Segments' axes topology

The modularity of symmetrical objects requires the introduction of separate axes of symmetry corresponding to the tower's segments (cf. left panel of **Fig. 3**). Parametrization of the entire structure requires a procedure that connects the estimated segments' axes. Given the axes' coefficients and the point cloud height range of the tower segments, the extreme and transitional points of the symmetry axes are identified. The extreme points are acquired by projecting the highest and lowest points from the cloud ($\boldsymbol{P}_{min}$ and $\boldsymbol{P}_{max}$) onto the axes of the lower (i=1 fot the segment #1) and upper (i=4 for the segment #4) parts of the tower:

$$\boldsymbol{P'}_{min} = \boldsymbol{P}_{i=1} + t_{min} \cdot \boldsymbol{V}_{i=1}, \tag{7}$$

$$\boldsymbol{P'}_{max} = \boldsymbol{P}_{i=4} + t_{max} \cdot \boldsymbol{V}_{i=4}, \tag{8}$$

where $t_{min} = (z_{\boldsymbol{P}_{min}} - z_{\boldsymbol{P}^{i=1}})/z_{\boldsymbol{V}^{i=1}}$ and $t_{max} = (z_{\boldsymbol{P}_{max}} - z_{\boldsymbol{P}^{i=4}})/z_{\boldsymbol{V}^{i=4}}$.

The coordinates of the transition points between the tower segments are calculated on the planes corresponding to the upper horizontal edges of the tower segments. This approach mitigates the limitation of the TLS point cloud occlusions caused by the ground-level measurements causing incomplete representation of the tower walls. The UAV point clouds provide better point coverage of inaccessible parts of the tower (**Fig. 5**).

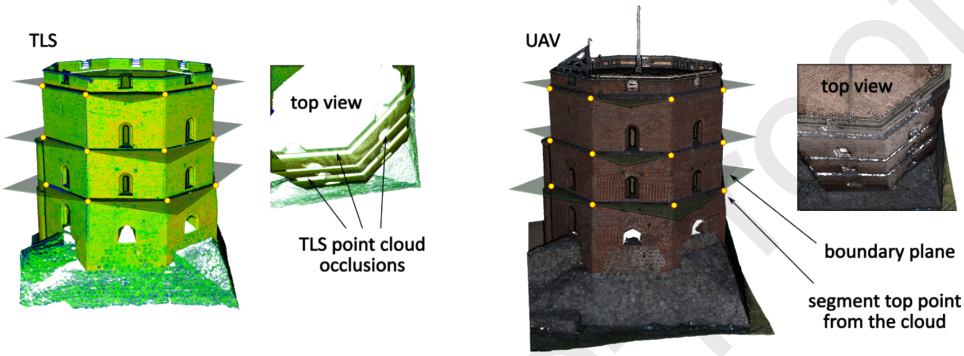

Fig. 5. Determination of transition planes between tower segments.

The points determined in the cloud were identified by analyzing the local normal vector gradient and the height coordinate. Three eight-element sets of points were determined for four segments. The PCA was used in each set to fit a quasi-horizontal plane $p_{i,i+1}$ given by the equation:

$$p_{i,i+1}: A_{i,i+1}x + B_{i,i+1}y + C_{i,i+1}z + D_{i,i+1} = 0, \tag{9}$$

where $i \in \langle 1,2,3 \rangle$ is the identifier of the tower segment.

The displacement of the tower segments' axes is defined by pairs of points representing the intersections of axes and transition planes:

$$\boldsymbol{Pb}_k^{i,i+1} = \boldsymbol{P}_{axis}^k - \frac{\boldsymbol{V}_{plane}^{i,i+1} \cdot \left(\boldsymbol{P}_{axis}^k - \boldsymbol{P}_{plane}^{i,i+1}\right)}{\boldsymbol{V}_{plane}^{i,i+1} \cdot \boldsymbol{V}_{axis}^k} \boldsymbol{V}_{axis}^k, \tag{10}$$

where $k \in \langle i, i+1 \rangle$, $\boldsymbol{P}_{axis}^k$ and $\boldsymbol{V}_{axis}^k$ denote the point and the vector defining the line, $\boldsymbol{P}_{plane}^{i,i+1}$ denotes the point on the transition plane, and $\boldsymbol{V}_{plane}^{i,i+1} = [A_{i,i+1} \quad B_{i,i+1} \quad C_{i,i+1}]^T$ denotes the normal vector of the transition plane $p^{i,i+1}$. The transition vectors $\boldsymbol{T}_{i,i+1}$ of the multi-modular axis of symmetry on the successive transition planes are obtained from the transition points $\boldsymbol{Pb}_k^{i,i+1}$:

$$\boldsymbol{T}_{i,i+1} = \boldsymbol{Pb}_{k=i+1}^{i,i+1} - \boldsymbol{Pb}_{k=i}^{i,i+1}. \tag{11}$$

2.2.3 Point cloud partitioning

A proposed element of symmetry in the HBIM of the towers with a regular polygon cross-section is the spatial configuration of the walls' vertical edges. The actual geometry of the building is compared with the theoretical shape. The symmetry assessment has two aspects. The first aspect of radial asymmetry of the tower edges includes a theoretical assumption of a constant angle between the planes containing the axis and consecutive walls' vertical edges. The second aspect concerns the course of the wall edges in relation to the estimated axis. Theoretically, all the vertical edges of the tower walls intersect at one point on the axis and each edge should create a separate plane with the axis of symmetry. In real conditions, the edges of the tower are deflected and are not co-planar with the axis.

The evaluation of the course of the wall edges is carried out using the Point Cloud Spatial Expansion (PCSE) method, which provides an alternative form of presentation of the geometry of symmetrical objects **[44]**. In the case of cylindrical PCSE, the primary surface is a cylinder with a radius corresponding to the size of the object. Structure deformations are obtained in the comparison of the length of the reference cylinder radius and the orthogonal distance of the point from the axis of symmetry. In the case of prismatic objects, e.g. towers with regular polygon cross-sections, the evaluation is more complex and involves the introduction of a reference prism and the assignment of points from a cloud to the appropriate walls of the solid **[45]**. An additional factor of the deformations assessment is the issue of axis verticality and modularity.

Previous historical tower geometry assessment methods are based on the division of the point cloud according to the interior angle of the cross-section octagon. For example, in the point cloud of the Tower of the Gediminas, eight parts of space corresponding to eight walls are determined. Each part of space is created by indicating two half-planes with a dihedral angle of $2\pi/N$, where N denotes the number of sides of the polygon. Each dividing half-plane shares the theoretical vertical axis of symmetry of the tower. However, this solution neglects the spatial asymmetry and deviation of the vertical edges of the tower walls. As a result, the obtained eight three-dimensional space orthants **[72]** introduce an error of assigning near-edge points to the wrong walls of the tower. The novel solution introduced in this study is to replace the fixed theoretical set of vertical half-planes with planes containing the actual vertical edge of the wall (**Fig. 6**).

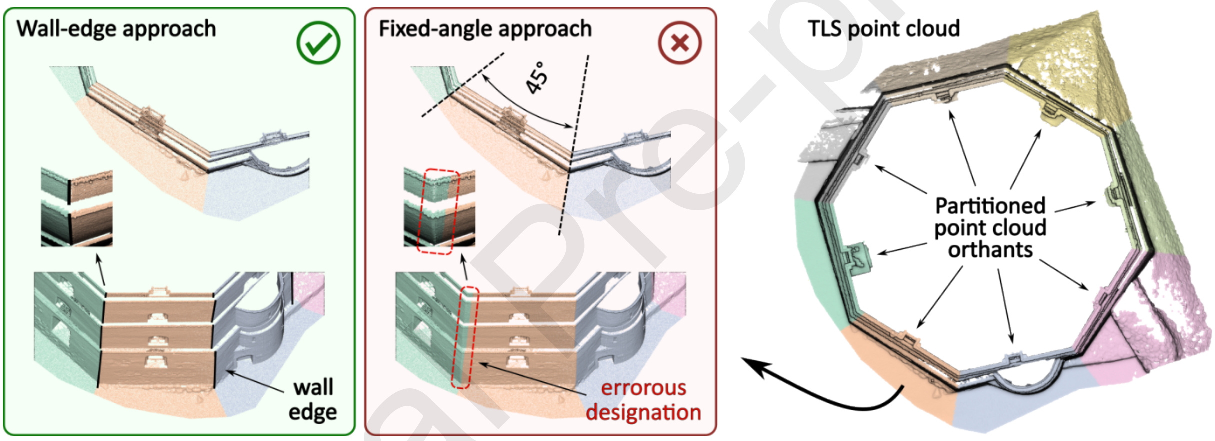

Fig. 6. Point cloud partitioning relative to the actual edges of the tower walls.

The presented solution provides the correct assignment of points to the tower walls. The eight parts of the three-dimensional Euclidean space are defined by the estimated wall edges (points $\boldsymbol{P}_{j,mod(j+1,N)}^{i}$ and vectors $\boldsymbol{V}_{j,mod(j+1,N)}^{i}$) and midpoints on the symmetry axis $\boldsymbol{Po}_i$. The midpoints are calculated between the extreme points $\boldsymbol{P'}_{min}$ and $\boldsymbol{P'}_{max}$ (**Eq. 7-8**) and points on the transition planes $\boldsymbol{Pb}_k^{i,i+1}$ (**Eq. 10**). For example, the midpoint on the second segment axis $\boldsymbol{Po}_2$ is calculated in the line segment $\overline{\boldsymbol{Pb}_{k=2}^{1,2}\boldsymbol{Pb}_{k=2}^{2,3}}$. Finally, the equation of the quasi-vertical division plane $q_{j,mod(j+1,8)}^{i}$ containing the vertical edge of the *j*-th and *mod(j+1)*-th walls at the *i*-th segment and the axis midpoint $\boldsymbol{Po}_i$ has the form:

$$q_{j,mod(j+1,N)}^{i}\colon A_{j,mod(j+1,N)}^{i}x + B_{j,mod(j+1,N)}^{i}y + C_{j,mod(j+1,N)}^{i}z + D_{j,mod(j+1,N)}^{i} = 0, \tag{12}$$

where $\left[A_{j,mod(j+1,N)}^{i} \quad B_{j,mod(j+1,N)}^{i} \quad C_{j,mod(j+1,N)}^{i}\right]^T = \boldsymbol{Vq}_{j,mod(j+1,N)}^{i} = \left(\boldsymbol{Po}_i - \boldsymbol{P}_{j,mod(j+1,N)}^{i}\right) \times \boldsymbol{V}_{j,mod(j+1,N)}^{i}$, and the last coefficient of the plane equation $D_{j,mod(j+1,8)}^{i}$ is the inverse of the sum of the products of the coordinates of the point $\boldsymbol{P}_{j,mod(j+1,N)}^{i}$ and the vector $\boldsymbol{Vq}_{j,mod(j+1,N)}^{i}$.

The position of a point from the cloud between two division planes $q_{j,mod(j+1,N)}^{i}$ determines the assignment to a tower wall. For example, for a wall panel with the identifier $j = 2$ located on a segment with the identifier $i = 1$ the condition takes the form:

$$\begin{cases} A_{1,2}^1 x + B_{1,2}^1 y + C_{1,2}^1 z + D_{1,2}^1 < 0 \\ A_{2,3}^1 x + B_{2,3}^1 y + C_{2,3}^1 z + D_{2,3}^1 \geq 0 \end{cases}. \tag{13}$$

The point-to-wall assignment is performed separately for each segment of the tower. The division of the point cloud into four horizontal segments (cf. **Fig. 3**) is performed manually or by the wall partitioning algorithm. In the second case, the logical condition (**Eq. 13**) is applied to the transition planes $p_{i,i+1}$ (**Eq. 9**). Both the lower and upper segments of the tower are exceptions where only one condition of two is applicable.

2.2.4 Point cloud cardinal orientation

The TLS point clouds, excluding the cases of using georeferencing markers, are described in an unknown local coordinate system. The application of the prismatic variant of the PCSE method requires the transformation of the point cloud to the state of parallelism of four of the eight faces with the directions of the orthogonal coordinate system. In our case, there are eight variants of rotation and a reasonable solution is the one that brings the point cloud to the orientation corresponding to the four geographical directions (N, S, E, W). As the directions of the tower walls in most cases do not coincide with the geographical directions, the angle of rotation called the cardinal orientation angle provides the smallest angular deviation of walls from the geographical directions.

The cardinal orientation requires prior verticalization of the point cloud, which eliminates the influence of the deflection of the estimated symmetry axes from the vertical. Omitting this calculation step causes significant errors in the PCSE expansion (cf. **[72]**). The multi-axial verticalization procedure is performed for each point in the cloud using the equation:

$$\boldsymbol{P}_{tmp}^{vert} = \boldsymbol{R}_Z(-\alpha_i) \cdot \boldsymbol{R}_Y\left({}^{\pi}/_{2} - \beta_i\right) \cdot \boldsymbol{R}_Z(\alpha_i) \cdot \left(\boldsymbol{P}_{tmp} - \boldsymbol{P'}_{min}\right) + \Delta\boldsymbol{T}, \tag{14}$$

where:

$\boldsymbol{P}_{tmp}^{vert}$ and $\boldsymbol{P}_{tmp}$ denote a point from the cloud after and before the verticalization procedure,

$\boldsymbol{R}_Y$ and $\boldsymbol{R}_Z$ denote elementary rotation matrices around the OY and OZ-axes,

$$\alpha_i = atan2(x_{\boldsymbol{V}_{axis}^i}, y_{\boldsymbol{V}_{axis}^i}) = \begin{cases} arctg\left(y_{\boldsymbol{V}_{axis}^i}/x_{\boldsymbol{V}_{axis}^i}\right) & for \quad (x_{\boldsymbol{V}_{axis}^i} > 0 \quad and \quad y_{\boldsymbol{V}_{axis}^i} \geq 0) \\ \pi/2 & for \quad (x_{\boldsymbol{V}_{axis}^i} = 0 \quad and \quad y_{\boldsymbol{V}_{axis}^i} \geq 0) \\ arctg\left(y_{\boldsymbol{V}_{axis}^i}/x_{\boldsymbol{V}_{axis}^i}\right) + \pi & for \quad x_{\boldsymbol{V}_{axis}^i} < 0 \\ 3\pi/2 & for \quad (x_{\boldsymbol{V}_{axis}^i} = 0 \quad and \quad y_{\boldsymbol{V}_{axis}^i} < 0) \\ arctg\left(y_{\boldsymbol{V}_{axis}^i}/x_{\boldsymbol{V}_{axis}^i}\right) + 2\pi & for \quad (x_{\boldsymbol{V}_{axis}^i} > 0 \quad and \quad y_{\boldsymbol{V}_{axis}^i} < 0) \\ undefined & for \quad (x_{\boldsymbol{V}_{axis}^i} = 0 \quad and \quad y_{\boldsymbol{V}_{axis}^i} = 0) \end{cases}, \text{ and}$$

$\beta_i = arccos\left(\sqrt{x_{\boldsymbol{V}_{axis}^i}^2 + y_{\boldsymbol{V}_{axis}^i}^2} / |\boldsymbol{V}_{axis}^i|\right)$ denote the rotation angles,

$\Delta\boldsymbol{T} = \sum_{s=1}^{i} \boldsymbol{T}_{s,s+1} + \boldsymbol{Pb}_{k=i}^{i,i+1} + \boldsymbol{T}_{i,i+1} - \boldsymbol{P'}_{min}$.

In the verticalization process, the point cloud is translated to the origin of the system using the coordinates of the axis points at the bottom of each segment (**Eq. 10**). Then, a sequence of elementary rotations brings the axes of symmetry to a vertical course. The verticalization procedure eliminates the object's inclination factor, maintains a horizontal orientation of the original point cloud, and enables reliable results of the PCSE method.

The cardinal orientation has two stages. In the first stage, the adjusted directions of tower vertices are estimated. Wall planes' normal vectors $\boldsymbol{N}_j^i$ were obtained by the RANSAC method (cf. **Section 2.2.1**). The LS estimation with the condition of a fixed theoretical interior angle of the octagon binding the parameters **[73]** is used to estimate horizontal directions**.** The obtained estimator $\hat{\mathbf{X}}_{dir}$ solves the conditional criterion of the objective function ψ which takes the form:

$$\psi(\boldsymbol{y},\hat{\mathbf{X}}_{dir}) = \boldsymbol{V}^T\boldsymbol{V} + \varepsilon\boldsymbol{\kappa}^{\boldsymbol{T}}(\boldsymbol{B}_{dir}\hat{\mathbf{X}}_{dir} + \boldsymbol{\Delta}) = \min_{\hat{\mathbf{X}}_{dir}}, \tag{15}$$

where:

$\boldsymbol{V}$ denotes the vector of the theoretical corrections with the expected value $E(\boldsymbol{V}) = \mathbf{0}$ such that $\boldsymbol{V} = \boldsymbol{A}_{dir}\hat{\mathbf{X}}_{dir} + \boldsymbol{L}_{dir}$, where $\boldsymbol{A}_{dir}$ denotes the matrix of derivatives and $\boldsymbol{L}_{dir} = \boldsymbol{y}^0 - \boldsymbol{y}$ denotes a vector of measured quantities, where $\boldsymbol{y}$, and $\boldsymbol{y}^0$ denote vectors of approximate measurement results determined from the basis of approximate values of the parametersdenotes the free-terms vector,

$\boldsymbol{B}_{dir}$ denotes the matrix of the coefficients of the conditional equations related to the parameter vector,

$\hat{\boldsymbol{\kappa}}$ denotes the vector of Lagrange multipliers such as $\hat{\boldsymbol{\kappa}} = -\left[\boldsymbol{B}_{dir}(\boldsymbol{A}_{dir}^T\boldsymbol{A}_{dir})^{-1}\boldsymbol{B}_{dir}^T\right]^{-1}\left[\boldsymbol{\Delta} - \boldsymbol{B}_{dir}(\boldsymbol{A}_{dir}^T\boldsymbol{A}_{dir})^{-1}\boldsymbol{A}_{dir}^T\boldsymbol{L}_{dir}\right]$, where $\boldsymbol{\Delta}$ is an additional conditional value vector.

The estimator $\hat{\mathbf{X}}_{dir}$ is determined by the formula:

$$\hat{\mathbf{X}}_{dir} = -(\boldsymbol{A}_{dir}^T\boldsymbol{A}_{dir})^{-1}(\boldsymbol{A}_{dir}^T\boldsymbol{L}_{dir} - \boldsymbol{B}_{dir}^T\hat{\boldsymbol{\kappa}}), \tag{16}$$

The detailed description of the calculation is presented in **[45]**. Finally, the direction closest to the *OX*-axis (θ) selected from the estimates vector $\hat{\mathbf{X}}_{dir}$ define the orientation of the tower with respect to the coordinate system. Angle θ is used to rotate the point cloud to meet the condition of parallelism of the four sides of the tower and the system's axes.

In the second stage of the cardinal orientation determination, the rotated point cloud is compared empirically with the actual geographic orientation of the tower. An additional *OZ*-axis rotation of the angle $c{\cdot}2\pi/N$ is introduced to position the point cloud according to the geographical directions. The value of the empirical coefficient c is adopted based on a satellite map, orthophotomap or georeferenced LiDAR data. Finally, the coordinates of the point after the cardinalization ($\boldsymbol{P}_{tmp}^{card}$) are obtained using the equation:

$$\boldsymbol{P}_{tmp}^{card} = \mathbf{R}_Z\left(2c\pi/N - \theta\right)\boldsymbol{P}_{tmp}^{vert}. \tag{17}$$

The algorithm of the cardinal orientation of the point cloud is presented in **Fig. 7**.

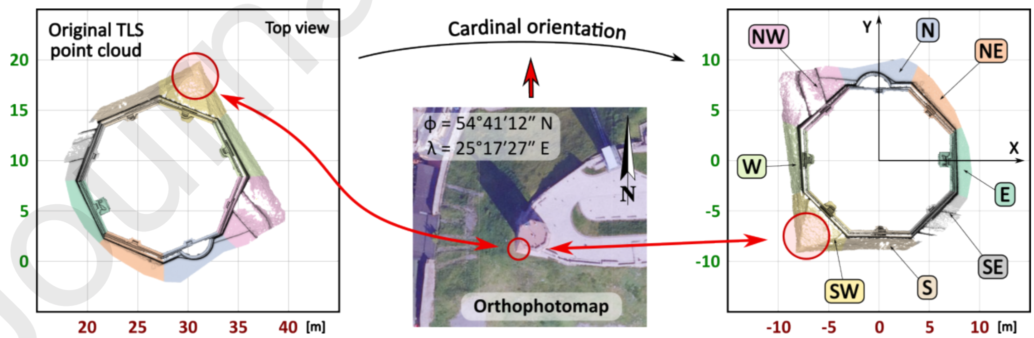

Fig. 7. Cardinal orientation of the TLS point cloud (map source: https://www.geoportal.lt/map/).

A feature of data from UAV LiDAR is the orientation of the point cloud based on the Earth-Centered Earth-Fixed (ECEF) coordinates in the WGS84 system **[74]** determined by the GNSS receiver. This ensures the preservation of four cardinal directions (N, S, E, W) in the point cloud of the measured object. Hence, the determination of the empirical parameter c is unnecessary as it takes the value of zero in (**Eq. 17**). The final result of the procedure is a verticalized and cardinally oriented point cloud. The introduction of a local coordinate system (right panel of **Fig. 7**) unifies the data gathered by different measurement techniques, eg. TLS and georeferenced ALS point clouds. Verticalization combined with the cardinal orientation provides a spatial harmonization of datasets with the requirement of the same linear unit. In this case study, the GNSS positional data are facultative additional attributes, connected with the directional angle θ that defines the historical building's location and radial orientation.

2.2.5 Point cloud spatial expansion

The principle of the PCSE method is to project the original point cloud relative to the adopted reference surface. However, the estimation of the parameters of the wall panels can be performed in the original point cloud, such an approach is not connected topologically with the historical object's multi-modal axis of symmetry. Determining the symmetry-oriented parameters requires joint processing of those two features, which is performed using the point cloud expansion methodology. PCSE functions perform coordinate transformation in the three-dimensional Euclidean space. The resulting expansion enables the geometric analyses that are not directly available in the original cloud, e.g. by introducing a depth parameter expressing the topology of a point relative to the adopted symmetry axis. Derived topological dependencies between the axis and points from the point cloud constitute the feature of automation of the PCSE in means of mass processing of the complex geometry of the historical object and providing a modified dataset for further analyses leading to the formulation and modeling of the HBIM symmetry parameters.

The prismatic variant of the PCSE method **[45]** was used on the point cloud of the Tower of the Gediminas. The dimensions of the reference prism are selected empirically for each object by analyzing the tower base, where its dimensions are the largest. The rounded radius of the circle circumscribed around the regular octagon of the lower cross-section of the tower base equaled $r = 9$ m. The methodology of the PCSE method involves assignment to individual space octants scalar variable η, whose value increases with the direction of the angle in the coordinate system (cf. right panel of **Fig. 7**). The eastern octant E receives the value $\eta = 0$, the next octant NE the value $\eta = 1$, and the last octant SE the value $\eta = 7$. The points from the cloud are assigned to individual octants based on the newly introduced analysis of the edges of the walls (**Eq. 13**) and not based on the fixed octagon interior angle criterion. The projection formulas of the prismatic PCSE have the form **[45]**:

$$\boldsymbol{P}_{tmp}^{PCSE}\left(\boldsymbol{P}_{tmp}^{vert}\right) = \boldsymbol{R}_X(\pi/2)\boldsymbol{R}_Z(\pi/2 + 2\eta\cdot\pi/N)\boldsymbol{P}_{tmp}^{vert} + [d(2N+1)/2 \quad 0 \quad -h]^T, \qquad (18)$$

where:

$\boldsymbol{P}_{tmp}^{PCSE}$ denotes a point from the cloud in the PCSE expansion,

$a = 2r\sin\left(\pi/N\right)$ denotes the length of the octagonal side of the reference prism,

$h = r\cos\left(\pi/N\right)$ denotes the length of the side's normal relative to the octagon center.

The result of application of the PCSE method on the TLS point cloud is presented in **Fig. 8**.

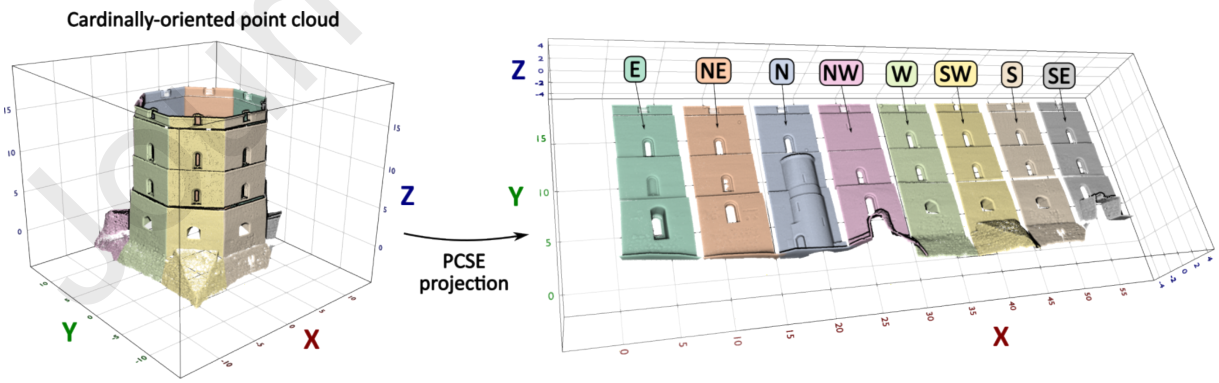

Fig. 8. Prismatic point cloud spatial expansion of the Tower of the Gediminas.

The advantage of the alternative form of presenting the tower geometry is obtaining additional geometric parameters describing the symmetry and deformations of the building. Changing the perspective view applied in the right panel of **Fig. 8** to the orthogonal *YZ*-plane side view, information about the course of all eight walls in relation to the axis of symmetry can be presented in a single view. The PCSE depth parameter (cf. **[44]** is a quantity related to the *z*-coordinate, which expresses the topology of the points and the reference prism. Thus, the depth parameter determines the deviation of points from the reference prism wall surface. This PCSE feature enhances the parameterization of a symmetrical structure for the HBIM.

2.3 HBIM asymmetry parametrization

The PCSE projection of the tower walls enables a unified comparison of the wall geometry. The wall-based assignment of points to the space orthants involves the differences in the width of tower walls. Additionally, the aspect of the asymmetric position of the tower walls' planes and edges can be assessed based on the PCSE depth parameter. The proposed HBIM symmetry parameters of towers with the geometry of a regular prism include:

- the course and orientation of the multi-modal axis of symmetry (HBIM axial factor),
- the planarity and inclination of the wall panels (HBIM wall panels' factor),
- the regularity of distribution of the wall edges ((HBIM wall edges' factor).

The proposed factors constitute a novel universal approach to present the aspect of symmetry of historical buildings in HBIM. The developed methodology can be used for objects with regular polygon cross-sections other than octagonal. The reports from the analyses enable effective assessment and localization of shape anomalies of tested objects. The procedure of conducting three HBIM analyses is presented in the following subsections.

2.3.1 HBIM axial factor

The symmetry characteristics of a historical building include the direction of the axes of individual tower segments represented by vectors $\boldsymbol{V}_{axis}^{i}$ and axis transition vectors $\boldsymbol{T}_{i,i+1}$. The vectors are given in the coordinate systems defined by a given sensor. TLS point clouds are combined into a single model in the registration process **[75]**. The registered point cloud adapts the coordinate system of one station as the global system and transforms the other scans. Presentation of the HBIM axial factor requires taking into account the cardinal orientation angle, which transforms the coordinates of the vectors $\boldsymbol{V}_{axis}^{i}$ and $\boldsymbol{T}_{i,i+1}$:

$$\boldsymbol{V}_{axis}^{i,card} = \boldsymbol{R}_Z\big(-2c\pi/N+\theta\big)\big(\boldsymbol{V}_{axis}^{i} - \boldsymbol{P'}_{min}\big), \tag{19}$$

$$\boldsymbol{T}_{i,i+1}^{card} = \boldsymbol{R}_Z\big(-2c\pi/N+\theta\big)\big(\boldsymbol{T}_{i,i+1} - \boldsymbol{P'}_{min}\big). \tag{20}$$

The direction of horizontal axis Hz_{axis}^{i} is defined relative to the cardinal orientation of the tower, i.e. not strictly relative to geographical directions (cf. **Subsection 2.2.4**). The direction of the axis is described by the equation:

$$Hz_{axis}^{i} = atan2\Big(x_{\boldsymbol{V}_{axis}^{i,card}}, y_{\boldsymbol{V}_{axis}^{i,card}}\Big) \cdot \rho, \tag{21}$$

where $\rho = 180°/\pi$ denotes the radial-to-degree angle conversion coefficient, and $atan2$ is the function described in (**Eq. 14**).

The deviation of the axis of symmetry from the vertical dV_{axis}^{i} is expressed by the quantity:

$$dV_{axis}^{i} = arccos\left(\frac{\boldsymbol{V}_{axis}^{i} \cdot \boldsymbol{V}_{OZ}}{\|\boldsymbol{V}_{axis}^{i}\|}\right) \cdot \rho, \tag{22}$$

where $\boldsymbol{V}_{OZ} = [0 \quad 0 \quad 1]^T$ denotes the vertical vector of the *OZ*-axis.

The deviation of the axis from the vertical dL_{axis}^{i} is unified by introducing the linear value of the horizontal displacement at the height interval of 1 m:

$$dL_{axis}^{i} = \frac{\sqrt{x_{\boldsymbol{V}_{axis}^{i}}^{2} + y_{\boldsymbol{V}_{axis}^{i}}^{2}}}{z_{\boldsymbol{V}_{axis}^{i}} \cdot \|\boldsymbol{V}_{axis}^{i}\|}. \tag{23}$$

2.3.2 HBIM wall panels' factor

The second HBIM factor of symmetry describes the geometry of the walls. Tower wall panels are presented in the PCSE in a unified way, taking into account the topology of the tower axis and the reference prism. The theoretical shape of the object includes a regular layout of walls and their uniform inclination. Considering the above statement in the context of PCSE, the projections of the tower wall panels should have a constant inclination in the *YZ*-plane (cf. right panel of **Fig. 8**). However, the actual state of the building differs from the theoretical model and the wall panels have various inclinations. Applying the RANSAC in the PCSE model space $i \cdot j$ fitted planes are obtained (**Eq. 1**), where the normal vector of the plane $\boldsymbol{N}_{PCSE_j^i} = \left[A_{PCSE_j^i}, B_{PCSE_j^i}, C_{PCSE_j^i}\right]^T$. The deviation of the normal vector from the wall-orthogonal direction is denoted as dN_j^i. Each of the RANSAC planes obtains a fitting error $RMS_{PCSE_j^i}$. The unit slope vector $\boldsymbol{S}_j^i$ is determined from the equation:

$$\boldsymbol{S}_j^i = \frac{\left(\boldsymbol{V}_{OZ} \times \boldsymbol{N}_{PCSE_j^i}\right) \times \boldsymbol{N}_{PCSE_j^i}}{\left\|\left(\boldsymbol{V}_{OZ} \times \boldsymbol{N}_{PCSE_j^i}\right) \times \boldsymbol{N}_{PCSE_j^i}\right\|}. \tag{24}$$

Additionally, it is reasonable to express the wall slope directions relative to the theoretical direction of the *OY*-axis. In theory, the PCSE wall slope vector dS_j^i contains in the *YZ*-plane, and its deviation is calculated from the relationship (cf. **Eq. 14**):

$$dS_j^i = \left(atan2\left(x_{S_j^i}, y_{S_j^i}\right) - \pi\right) \cdot \rho. \tag{25}$$

The HBIM wall panels' factor evaluation performed on the TLS data is presented in **Fig. 9**.

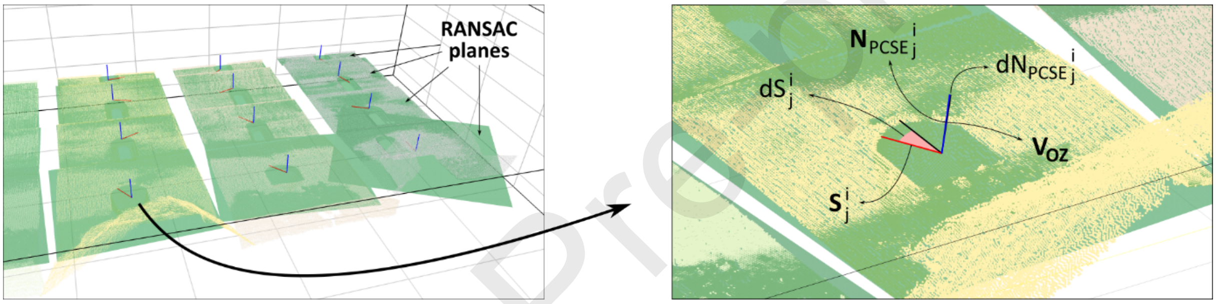

Fig. 9. Factor of wall symmetry estimated in the TLS point cloud.

2.3.3 HBIM wall edges' factor

The third HBIM factor of symmetry is related to the course of the wall edges. The analysis is conducted in two aspects. The first aspect concerns the radial position, and the second is the linear displacements of the tower wall edges. The actual state of the tower is compared with the theoretical course of the wall edges derived from the shape of the reference prism. The radial assessment describes the regularity of distribution of the wall edges. The linear assessment focuses on the repeatability of the wall lengths and the distances of the wall edges from the prism of reference.

Theoretical wall slope estimation begins with fitting four longitudinal planes into the merged sets of eight PCSE projections of the wall panels in four tower segments. The crucial feature of the PCSE depth parameter is the parametrization of the distance of points to the reference prism walls (**Eq. 18**). Points located at the base of the tower are closest to the prism walls, which implies smaller PCSE depth parameter values compared to points located higher on the tower wall surface. The reference plane of the *i*-th tower segment with coefficients A_{ref}^i, B_{ref}^i, C_{ref}^i, and D_{ref}^i is obtained using the LS estimation.

The A_{ref}^i coefficient of the tower segments' reference planes theoretically should equal zero as it is independent of the coordinate of the *OX*-axis. However, different inclinations of individual wall panels in PCSE cause this condition to be not met. The identification of a constant inclination of the reference plane mitigating the influence of minor deflections of wall panels is carried out by calculating the theoretical values of the PCSE depth parameter at the bottom and top of each panel at the center of the PCSE expansion ($x_{PCSE}^{mid} = 4a$). This coordinate corresponds to the center point of the perimeter of the prism cross-section.

The theoretical course of the edges of the eight tower walls is determined in the PCSE based on the calculated reference planes of the segments. The z_{PCSE} coordinates of the lower (*bot*) and upper (*top*) points defining the course of the wall edges are determined from the equations:

$$z_{PCSE}^{i,bot} = \left[x_{PCSE}^{mid} \quad z_i^{bot} \quad -\left(z_i^{bot} \cdot B_{ref}^i + D_{ref}^i\right) / C_{ref}^i\right]^T, \tag{26}$$

$$z_{PCSE}^{i,top} = \left[x_{PCSE}^{mid} \quad z_i^{top} \quad -\left(z_i^{top} \cdot B_{ref}^i + D_{ref}^i\right) / C_{ref}^i\right]^T, \tag{27}$$

where z_i^{bot} and z_i^{top} denote the coordinates of the points $\boldsymbol{P'}_{min}$ i $\boldsymbol{P'}_{max}$ (**Eq. 7-8**) and the points $\boldsymbol{Pb}_k^{i,i+1}$ (**Eq. 10**) defining the axis of symmetry on the *i*-th segment of the tower. For each segment, the upper and lower points are selected according to the **Section 2.2.2**.

The theoretical slope of the edges of walls is determined based on the PCSE depth parameter (coordinates $z_{PCSE}^{i,bot}$ and $z_{PCSE}^{i,top}$). The next stage of calculations is to indicate the theoretical position of the edges in PCSE along to *OX*-axis. Based on the geometry of the reference prism, the value of the angle between the successive edges is known and equals for the octagonal structures $\sigma = 2\pi/N = \pi/4$, where $N = 8$. Each of the eight walls is limited by two vertical edges, so sixteen PCSE edges of theoretical walls are determined. The coordinates of the points $\boldsymbol{E}_{PCSE}^{i,bot}$ and $\boldsymbol{E}_{PCSE}^{i,top}$ defining the course of the edges are determined from the equation:

$$\boldsymbol{E}_{PCSE}^{i,bot} = \begin{bmatrix} \left(h + z_{PCSE}^{i,bot}\right) / \cos\left(\pi/N\right) \cos\left(\pi/N + i\sigma\right) \\ \left(h + z_{PCSE}^{i,bot}\right) / \cos\left(\pi/N\right) \sin\left(\pi/N + i\sigma\right) \\ z_{PCSE}^{i,bot} \end{bmatrix}, \tag{28}$$

$$\boldsymbol{E}_{PCSE}^{i,top} = \begin{bmatrix} \left(h + z_{PCSE}^{i,top}\right) / \cos\left(\pi/N\right) \cos\left(\pi/N + i\theta\right) \\ \left(h + z_{PCSE}^{i,top}\right) / \cos\left(\pi/N\right) \sin\left(\pi/N + i\theta\right) \\ z_{PCSE}^{i,top} \end{bmatrix}. \tag{29}$$

The actual course of the wall edges is defined by points $\boldsymbol{P}_{j,mod(j+1,N)}^i$ and direction vectors $\boldsymbol{V}_{j,mod(j+1,N)}^i$ (**Eq. 2-3**). The coordinates of the points on the actual edges are calculated using the following formulas:

$$\boldsymbol{F}_{PCSE}^{i,bot} = \boldsymbol{P}_{j,mod(j+1,N)}^i + t_{i,\,bot} \cdot \boldsymbol{V}_{j,mod(j+1,N)}^i, \tag{30}$$

$$\boldsymbol{F}_{PCSE}^{i,top} = \boldsymbol{P}_{j,mod(j+1,N)}^i + t_{i,\,top} \cdot \boldsymbol{V}_{j,mod(j+1,N)}^i, \tag{31}$$

where $t_{i,\,bot} = \left(z_i^{bot} - z_{\boldsymbol{P}_{j,mod(j+1,N)}^i}\right) / z_{\boldsymbol{V}_{j,mod(j+1,N)}^i}$ and $t_{i,\,top} = \left(z_i^{top} - z_{\boldsymbol{P}_{j,mod(j+1,N)}^i}\right) / z_{\boldsymbol{V}_{j,mod(j+1,N)}^i}$. The desidentifiers of the left and right sides at the upper and lower edges have been omitted to avoid complicating the formulas.

The lengths of horizontal wall edges and the position of the walls' vertical axes are determined in PCSE. The length deviation of the lower edge of the wall is expressed both in linear and relative forms:

$$dL_{PCSE}^{i,bot} = \left(x_{\boldsymbol{F}_{PCSE}^{i,bot}}^{right} - x_{\boldsymbol{F}_{PCSE}^{i,bot}}^{left}\right) - \left(x_{\boldsymbol{E}_{PCSE}^{i,bot}}^{right} - x_{\boldsymbol{E}_{PCSE}^{i,bot}}^{left}\right), \tag{32}$$

$$\overline{dL}_{PCSE}^{i,bot} = \left[\left(x_{\boldsymbol{F}_{PCSE}^{i,bot}}^{right} - x_{\boldsymbol{F}_{PCSE}^{i,bot}}^{left}\right) - \left(x_{\boldsymbol{E}_{PCSE}^{i,bot}}^{right} - x_{\boldsymbol{E}_{PCSE}^{i,bot}}^{left}\right)\right] \Big/ \left(x_{\boldsymbol{E}_{PCSE}^{i,bot}}^{right} - x_{\boldsymbol{E}_{PCSE}^{i,bot}}^{left}\right) \cdot 100\%. \tag{33}$$

The relative deviation $\overline{dL}_{PCSE}^{i,bot}$ corresponds to the theoretical length of the wall and is determined in percentages. Analogous calculations are performed for the upper walls of the tower.

Radial evaluation requires determining the vertical axes of the walls represented by the midpoints of the upper and lower wall edges. In the case of theoretical data, the points $\boldsymbol{G}_{PCSE}^{i,bot}$ are obtained, and in the case of actual data $\boldsymbol{H}_{PCSE}^{i,bot}$. The deviation of the axis position at the bottom wall edge is expressed in both the linear and the angular values:

$$dM_{PCSE}^{i,bot} = \boldsymbol{H}_{PCSE}^{i,bot} - \boldsymbol{G}_{PCSE}^{i,bot}, \tag{34}$$

$$\delta_{PCSE}^{i,bot} = \text{arctg}\left(dM_{PCSE}^{i,bot} / \left(z_{\boldsymbol{E}_{PCSE}^{i,bot}} + h \right) \right) \cdot \rho. \tag{35}$$

The angular deviation $\delta_{PCSE}^{i,bot}$ is calculated in the triangle formed by the theoretical ($\boldsymbol{G}_{PCSE}^{i,bot}$) and actual ($\boldsymbol{H}_{PCSE}^{i,bot}$) center of the wall edge, and the height-dependent distance of the wall axis from the tower symmetry axis. The determined geometrical quantities are presented in **Fig. 10**.

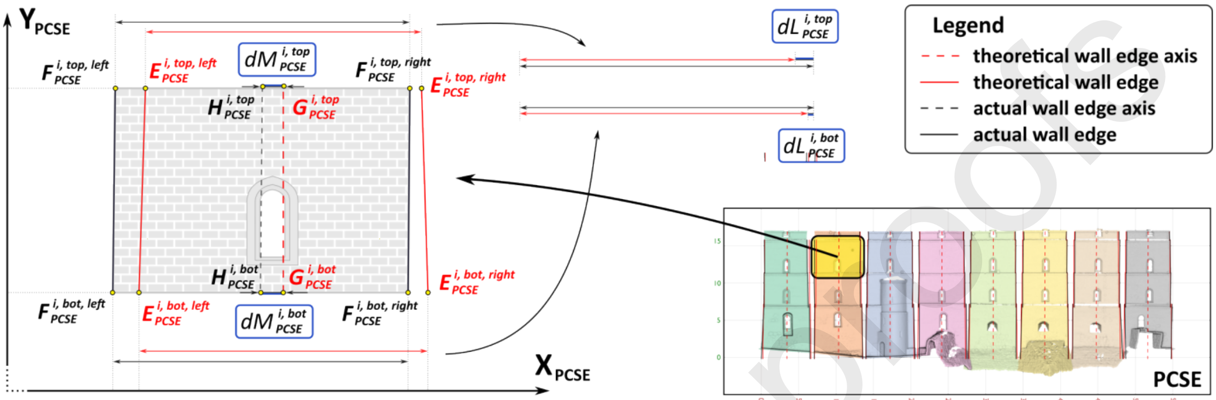

Fig. 10. Wall edges factor components.

The last element of the tower edge analysis is the comparison of the values of the PCSE depth parameter of the extreme edge points. In the case of the theoretical model, the inclination of all eight walls on a given tower segment is the same, which results in the fixed values of the PCSE depth parameter (z_{PCSE}) for a given value of the y_{PCSE} coordinate. Meanwhile, in the actual model, the course of the edge is different, which results in different distances of the edge points from the reference prism. The deviations are calculated separately for each point on the edge taking into account the theoretical shape of each wall. For example, the deviation for the left point at the bottom edge of the wall is determined from the equation:

$$dz_{PCSE}^{i,bot,left} = z_{\boldsymbol{F}_{PCSE}^{i,bot}}^{left} - z_{\boldsymbol{E}_{PCSE}^{i,bot}}^{left}. \tag{36}$$

Summing up, the components of the HBIM wall edges' factor are: linear (dL) and relative (($\overline{dL}$) deviation of the length of the wall edges, linear (dM) and angular (δ) deviation of the position of the wall axes, and deviations of the PSCE depth parameter of the wall edge points (dz_{PCSE}).

3 Results

3.1 HBIM symmetry datasheet

Symmetry parameters of the Tower of the Gediminas in Vilnius were determined based on TLS data. **Subsection 3.2** presents a comparative analysis of competitive parameters calculated for the UAV model. The first element of the HBIM symmetry parameterization is the axial factor representing the topology of the tower's symmetry axis on four segments (**Fig. 11**).

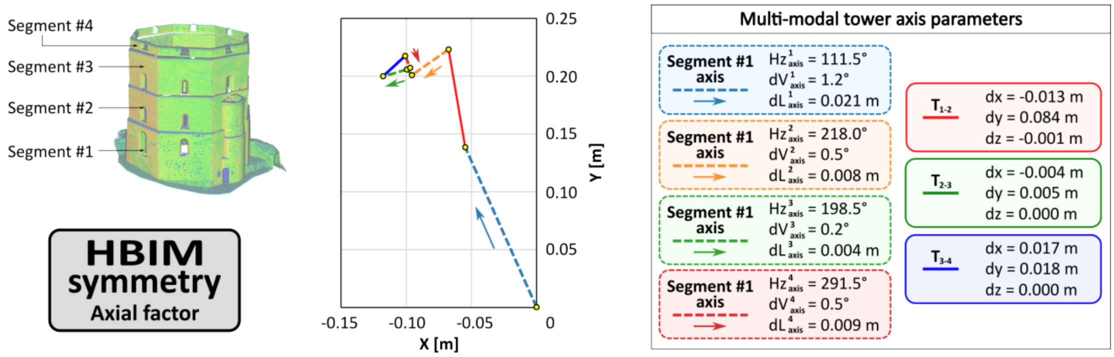

Fig. 11. HBIM axial factor of the Tower of the Gediminas.

The directional arrows placed at the axes (dashed lines) indicate the increase in the height coordinate. The displacements on transition planes between the end point of the lower segment axis and the starting point of the upper segment axis are described by vectors $\boldsymbol{T}_{i,i+1}$. Each component of the multi-modular axis of symmetry is defined by the horizontal orientation of the axis (Hz^i_{axis}), the deviation of the axis from the vertical direction (dV^i_{axis}), and the unified linear value of the axis horizontal displacement over a 1 m interval of height change (dV^i_{axis}).

The second element of the HBIM symmetry parameterization is the wall panels' factor presenting the features of the tower wall planes on subsequent segments (**Fig. 12**).

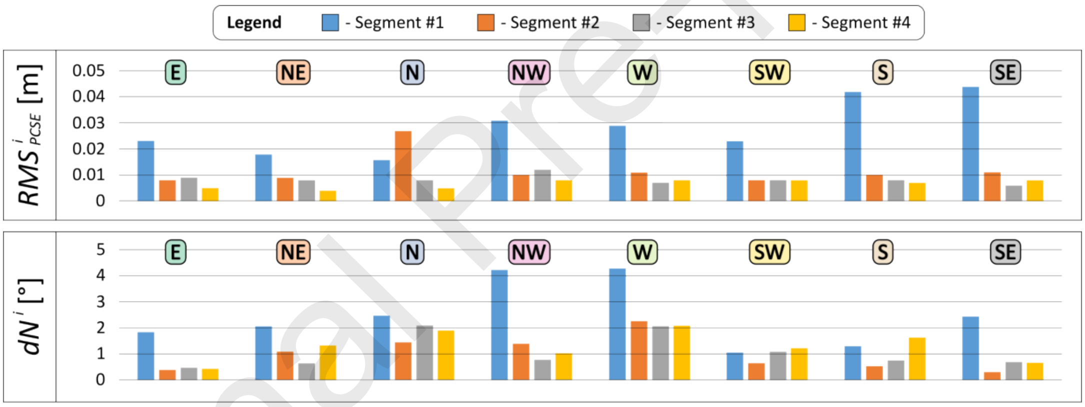

dS^i [°] Segment	E	NE	N	NW	W	SW	S	SE
#1	301.3°	57.1°	305.4°	57.1°	292.6°	33.0°	39.6°	0.7°
#1	212.7°	63.2°	48.8°	103.5°	275.3°	297.1°	37.5°	63.9°
#1	271.0°	70.8°	109.1°	119.6°	272.8°	256.5°	111.6°	200.0°
#1	344.6°	135.1°	107.6°	157.4°	257.5°	282.7°	132.5°	200.6°

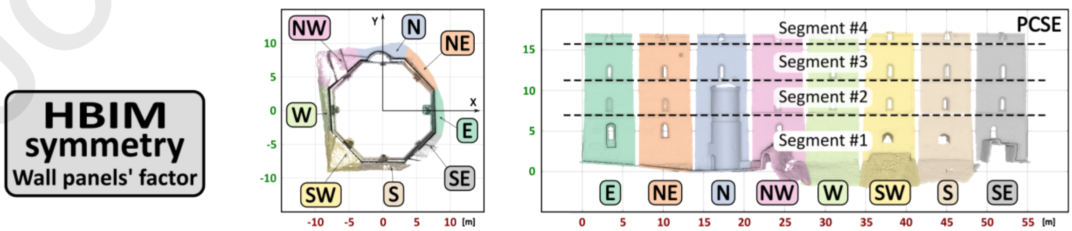

Fig. 12. HBIM wall panels' factor of the Tower of the Gediminas.

The lower panel of the figure represents the layout of the tower sides and corresponds to three upper tables containing the following parameters: the RANSAC fitting error of the wall point cloud ($RMS_{PCSE^i_j}$), the deviation of the wall-normal vector from the orthogonal direction (dN^i_j), and the direction of the wall slope vector (dS^i_j). The chart presents the geometry of the tower walls calculated according to the methodology of **Section 2.3.2**.

The third element of the HBIM symmetry parameterization is the wall edges' factor, which presents the geometric parameters of the tower wall edges compared with the theoretical reference prism shape. The evaluated parameters are: the relative deviation of the length of the upper ($\overline{dL}_{PCSE}^{i,top}$) and lower $\overline{dL}_{PCSE}^{i,bot}$) wall edges, the angular deviation of the wall axis position ($\delta_{PCSE}^{i,top}$ and $\delta_{PCSE}^{i,bot}$), and the deviation of the PCSE depth parameter of the left ($dz_{PCSE}^{i,bot,left}$ and $dz_{PCSE}^{i,top,left}$) and right ($dz_{PCSE}^{i,bot,right}$ and $dz_{PCSE}^{i,top,right}$) wall edges. The method of including multiple parameters for each tower wall is presented in **Fig. 13**.

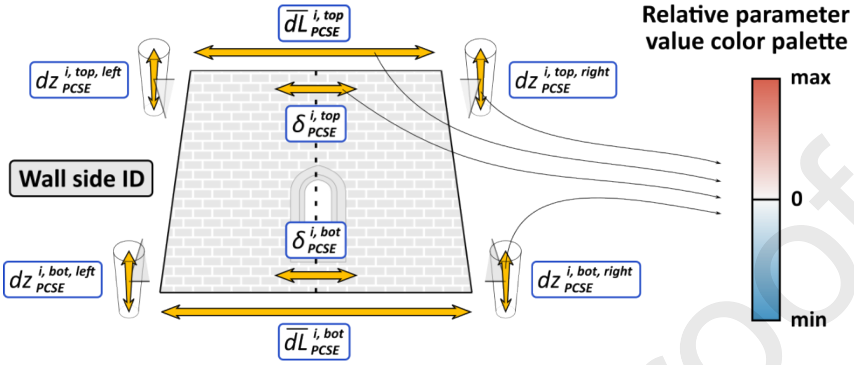

Fig. 13. HBIM wall edges' factor of the Tower of the Gediminas.

The parameter values are located near the arrows representing the wall edge width (top and bottom arrows), the angular offset of the wall symmetry axis (two middle arrows), and the PCSE depth parameter offset in the direction perpendicular to the wall (four external arrows). The parameter value obtains the colors from a uniform color palette. Such an approach enables an efficient evaluation of the parameters' values for the multiple tower walls' panels (**Fig. 14**).

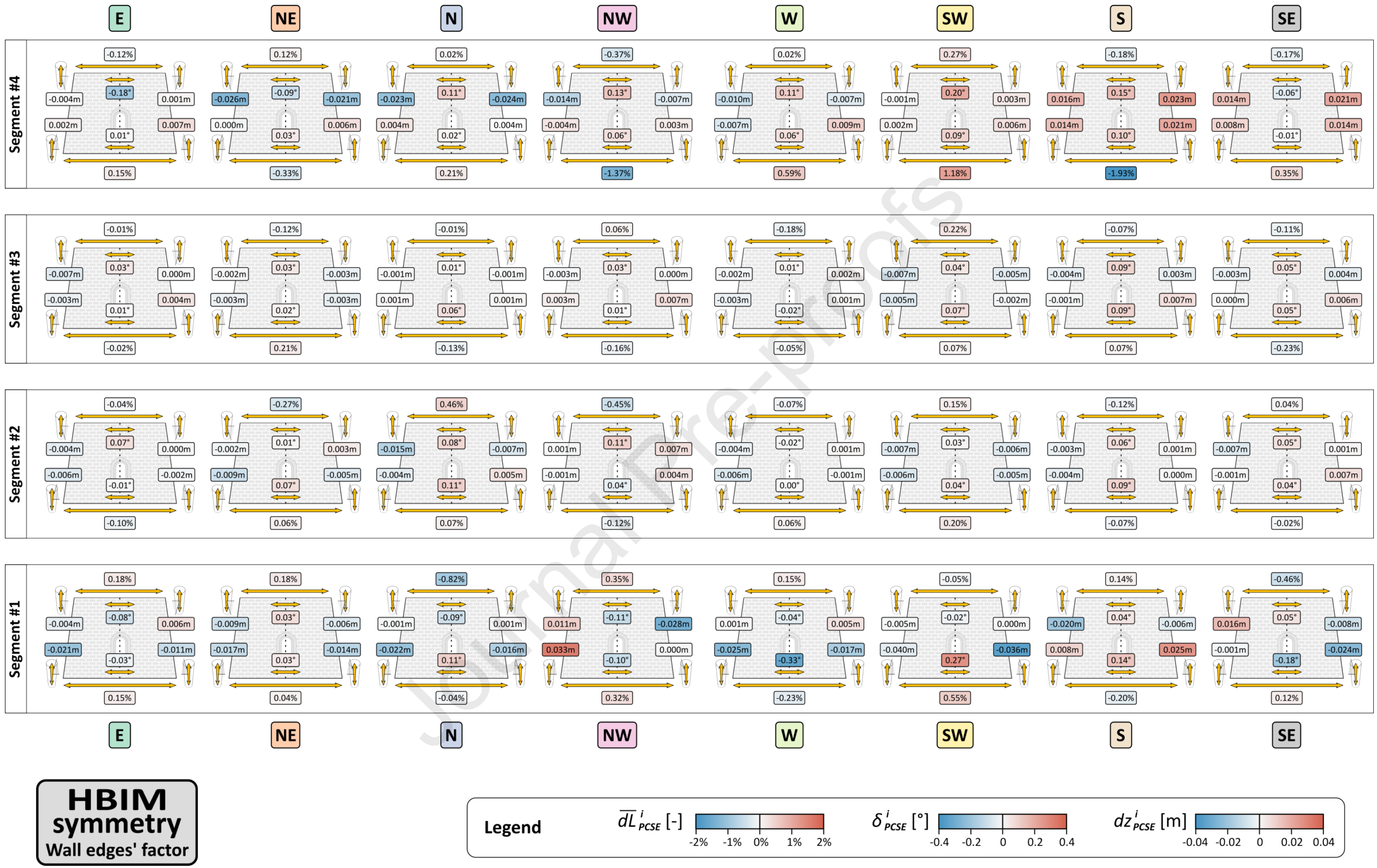

Fig. 14. HBIM wall edges's factor of the Tower of the Gediminas.

The graph indicates the major asymmetry of the highest and lowest segments of the Tower of the Gediminas, especially on the southern and eastern walls. The middle segments of the tower are characterized by moderate asymmetry parameters. The extreme radial deviations of the wall axes (δ^i_{PCSE}) deviate from the theoretical reference positions by no more than 0.4°. The relative deviations of the width of the horizontal edges of the walls ($\overline{dL}^i_{PCSE}$) do not exceed 2%. The differences in the depth parameter PCSE (dz^i_{PCSE}) are in the range from -4 to 4 cm. The statistical analysis of the results is presented in **Tab. 1**.

Tab. 1. Statistical parameters of the absolute values of selected HBIM parameters for the Gediminas Tower determined for the TLS model.

Parameter location		$\lvert\overline{dL}^i_{PCSE}\rvert$[m]	$\lvert\delta^i_{PCSE}\rvert$[°]	$\lvert dz^{i,left}_{PCSE}\rvert$[m]	$\lvert dz^{i,right}_{PCSE}\rvert$ [m]
segment #1	top	0.018 ± 0.015	0.008 ± 0.004	0.008 ± 0.007	0.008 ± 0.008
	bottom	0.049 ± 0.039	0.020 ± 0.014	0.021 ± 0.012	0.018 ± 0.010
segment #2	top	0.012 ± 0.010	0.007 ± 0.004	0.005 ± 0.004	0.003 ± 0.003
	bottom	0.007 ± 0.004	0.006 ± 0.005	0.005 ± 0.003	0.004 ± 0.002
segment #3	top	0.006 ± 0.004	0.005 ± 0.003	0.004 ± 0.002	0.002 ± 0.002
	bottom	0.005 ± 0.003	0.005 ± 0.004	0.002 ± 0.002	0.004 ± 0.002
segment #4	top	0.009 ± 0.006	0.016 ± 0.005	0.013 ± 0.008	0.013 ± 0.009
	bottom	0.012 ± 0.009	0.006 ± 0.004	0.005 ± 0.004	0.009 ± 0.006

3.2 TLS and UAV data validation

This section containes the comparison of the HBIM parametrization results obtained in two competitive point cloud models. The gathered TLS and UAV point clouds of the Tower of the Gediminas in Vilnius were clipped and filtered to eliminate outliers **[76]**. In the next step, the point cloud fragments containing four segments of the tower were selected and the RANSAC method was used to identify sets of eight tower wall panels in each segment (cf. **Fig. 3**). The RMS errors of the fitted planes are summarized in **Tab. 2**.

Tab. 2. RANSAC RMS UAV-TLS wall planes differences.

Tower segment	**Wall plane RMS difference [mm]**							
	E	**NE**	**N**	**NW**	**W**	**SW**	**S**	**SE**

#1	0.3	0.1	2.5	3.9	-1.4	-0.6	-3.5	3.6
#2	0.2	-0.1	3.5	-1.8	-0.2	1.7	-1.9	0.1
#3	-0.4	-0.4	1.0	-1.5	-1.7	1.3	-3.3	-0.7
#4	-0.7	0.3	1.6	0.0	-1.5	0.2	0.0	-0.7

The comparison showed that the results for both methods were consistent by a few millimeters. The mean RMS error difference for all segments was 1.3 mm with a standard deviation of 1.0 mm. The largest mean error (2.0 ± 1.5 mm) occurred for the bottom segment #1. Analyzing each wall panel separately eliminates the problem of absolute accuracy of several centimeters of the UAV LiDAR point cloud. The obtained RMS values show that the limited number of points in the UAV data is sufficient for obtaining estimates differing by a few millimeters from the dense TLS data, which indicates the high precision of both datasets and robustness of the estimation approach.

The next step of the calculations was the estimation of the course of the tower's axis using the new approach based on the planes of the walls of a symmetrical prismatic structure. To compare and demonstrate the validity of the new method of axis determination, a calculation based on the sets of horizontal cross-sections was performed. In the TLS point cloud, 11, 10, 11, and 5 cross-sections were extracted on four tower segments, respectively. In the UAV point cloud, the sets consisted of 8, 10, 10, and 4 cross-sections, respectively. The differences in parameter values are presented in **Tab. 3**.

Tab. 3. Comparison of the axes estimated based on wall planes and point cloud cross-sections approaches.

Axes fit parameter	**Segment #1**		**Segment #2**		**Segment #3**		**Segment #4**	
	TLS	**UAV**	**TLS**	**UAV**	**TLS**	**UAV**	**TLS**	**UAV**
RMS Walls [m]	4.8E-05	1.5E-05	8.5E-06	1.4E-05	6.0E-06	5.2E-06	1.2E-06	8.1E-07
RMS Sections [m]	7.1E-03	1.2E-02	9.0E-04	1.9E-03	1.1E-03	7.5E-04	1.4E-03	4.4E-04
Angle [°]	0.252	0.606	0.044	0.083	0.002	0.024	0.247	0.075

The mean values of the RMS errors of the wall-planes approach did not exceed 1% of the mean errors calculated for the cross-sections. The probable cause is a limited number of wall points used in the cross-section approach, while in the second case involving planes all points belonging to a given tower wall are used in the RANSAC estimation. Additionally, the angles between the vectors of both estimated axes from the TLS model, apart from the narrow segment #4, are several times smaller than in the case of UAV data. The deviations between the axis courses determined using planes and cross-sections appraoaches do not exceed 0.25°, apart from the most irregular segment #1 of the tower.

The multi-modal axis topology is determined by the symmetry axes of the four tower segments and the axis transition vectors at the boundary planes (cf. **Section 2.2.2**). The HBIM symmetry parameters obtained for the TLS and UAV data are compared in **Tab. 4**.

Tab. 4. TLS and UAV HBIM axial factor differences of the Tower of the Gediminas.

	Parameter	Segment #1	Segment #2	Segment #3	Segment #4
Axis	Hz^i_{axis} **[°]**	-3.52	8.51	2.91	-15.88
	dV^i_{axis} **[°]**	-0.11	0.09	-0.01	-0.12
	dL^i_{axis} **[mm]**	-1.8	1.6	-0.1	-2.1
		$\boldsymbol{T}_{1,2}$	$\boldsymbol{T}_{2,3}$	$\boldsymbol{T}_{3,4}$	
Vector	dx **[mm]**	-2.5	-2.5	2.0	
	dy **[mm]**	7.4	5.5	2.0	
	dz **[mm]**	0.6	0.0	-0.1	

The directions of the tower symmetry axis (dV^i_{axis}) differed in the three cases by ca. 0.1° (segments #1, #2, and #4), which translates into a horizontal shift (dL^i_{axis}) of a few millimeters at a relative distance of 1 m. The absolute value of the difference in the horizontal axis orientation (Hz^i_{axis}) for the three lower segments of the tower did not exceed 10°. The higher parameter value for segment #4 (-15.88°) is associated with the smallest height range of the top segment of the tower and the limitations of the TLS scanning method implied by the incomplete coverage of the walls of the tower's upper segment. The differences in the coordinates of the axis shift vectors at the boundary planes ($\boldsymbol{T}_{i,i+1}$) did not exceed 8 mm. Summing up the analysis of the axis topology, the low values of the HBIM parameter differences confirm the high convergence of the TLS and LiDAR UAV sensor data.

The comparison of the HBIM wall panel's factor values determined for TLS and UAV data is presented in **Tab. 5**. The methodological description of the parameters was presented in **Subsection 2.3.2**.

Tab. 5. TLS and UAV differences in the HBIM wall panel's factor of the Tower of the Gediminas.

Wall side	Segment #1			Segment #2			Segment #3			Segment #4		
	RMS [m]	dN^i_j**[°]**	dS^i_j**[°]**	**RMS [m]**	dN^i_j**[°]**	dS^i_j**[°]**	**RMS [m]**	dN^i_j**[°]**	dS^i_j **[°]**	**RMS [m]**	dN^i_j**[°]**	dS^i_j**[°]**
E	-0.002	0.10	3.20	0.001	0.08	0.90	0.000	0.06	0.96	0.000	-0.18	-123.58
NE	0.000	0.00	-2.08	0.000	-0.08	3.72	0.001	-0.02	1.10	0.001	-0.23	-8.94
N	0.001	0.01	-1.94	0.002	-0.11	0.04	0.000	0.03	1.74	0.001	-0.10	-13.05
NW	0.000	-0.05	0.45	-0.001	-0.03	6.36	0.000	-0.02	10.26	-0.001	-0.18	-0.37

W	-0.002	0.00	-0.68	-0.001	0.05	-0.70	-0.002	0.05	-1.86	-0.002	0.08	-4.79
SW	-0.001	-0.08	0.01	0.000	0.05	6.10	0.001	0.01	1.68	0.001	0.14	-40.03
S	-0.004	0.30	-14.75	-0.002	0.02	-11.85	-0.003	-0.06	3.64	0.000	1.24	24.45
SE	-0.002	0.25	-1.50	0.000	-0.01	-12.39	0.000	0.06	1.56	-0.001	1.39	-12.22

Similarly to the case of RANSAC plane fitting in the original point cloud (cf. **Fig. 3** and **Tab. 2**), the RMS differences of the plane fitting in PCSE took values of single millimeters. In one case, the RMS difference between TLS and UAV data took the value of -0.004 m. The remaining RMS differences most often took values of 0 or 1 mm. The differences in the deviation of the plane normal vector in PCSE from the vertical direction (dN_j^i) in absolute values had an average value of 0.16° with a standard deviation of 0.31°. It should be noted here the influence of much larger differences of the parameter for the highest segment #4 of the tower. A similar case occurred in comparison of the direction of plane slope in PCSE (dS_j^i), where most walls of segment #4 obtained differences significantly exceeded the table's threshold value of 10°. In the remaining cases, the TLS and UAV data differences in the parameter dS_j^i had a significantly lower mean value of 3.7° with a standard deviation of 4.2°. A potential reason for these differences is the different degree of tower coverage by points in both data sets.

The comparison of TLS and UAV data HBIM wall edges' factor values is presented in **Fig. 15** and **Fig. 16**. In the analysis of the course of the walls' edges of the Gediminas tower, the width of the lower and upper wall edges (dL_{PCSE}^i and $\overline{dL}_{PCSE}^i$), the position of the vertical center axis of each wall (dM_{PCSE}^i and δ_{PCSE}^i), and the distances of the edges relative to the reference prism ($dz_{PCSE}^{i,left}$ and $dz_{PCSE}^{i,right}$) were assessed. The listed parameters are presented without the identifiers of the lower (*bot*) and upper (*top*) wall edges. Due to the large amount of analyzed data, the results of the comparison of the TLS and UAV parameters are presented in graphs. The differences in parameter values are calculated for each of the eight sides on four tower segments (left panel of **Fig. 15**). Then, the results for tower segments were statistically evaluated (right panel of **Fig. 15**).

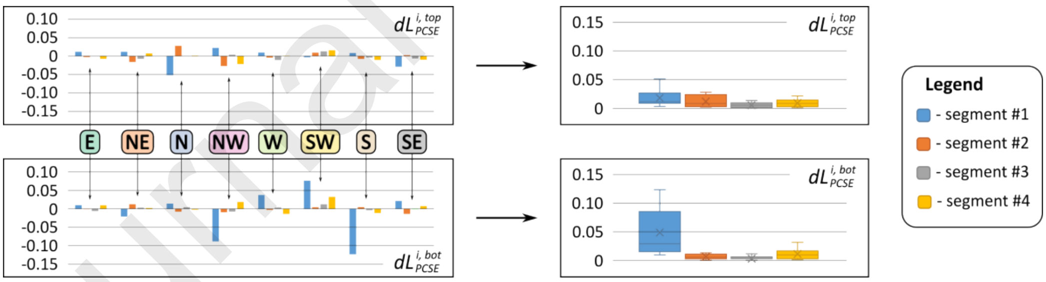

Fig. 15. Distribution of differences in the lengths of the upper and lower edges determined from the TLS and UAV data.

The presented evaluation algorithm enables the indication of repeatable trends in both the TLS and UAV results. For example, the difference in the tower wall width parameter (dL_{PCSE}^i) presented in **Fig. 15** indicates significantly greater differences at the bottom edge of the wall of segment #1 ($dL_{PCSE}^{1,bot}$). In the relative percentage terms including the edge length ($\overline{dL}_{PCSE}^{i,bot}$), the largest differences between the TLS and UAV data occurred at the bottom of segment #1 and amounted to an average of 0.76% ± 0.61% of the entire edge length. The remaining tower segments achieved mean values of linear deviations $dL_{PCSE}^{i,bot}$ at their lower edges not greater than 0.01 m ± 0.01 m. In the case of the upper edge, the differences in the mean value $\overline{dL}_{PCSE}^{i,top}$ achieved values from a smaller range from 0.10% (segment #3) to 0.20% (segment #1), which in a linear measure corresponds to values from 0.01 m ± 0.004 m to 0.02 m ± 0.01 m (upper right panel of **Fig. 15**).

The differences in the remaining HBIM wall panel's edge parameters were subjected to a similar calculation process (**Fig. 16**).

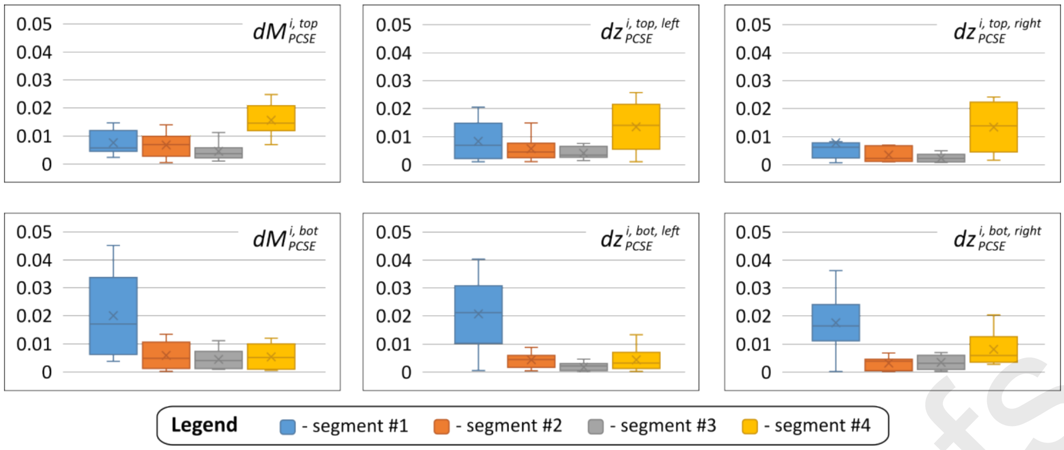

Fig. 16. Distribution of TLS and UAV data differences in the axis position deviation (left panel), differences in the PCSE depth parameter of the left (middle panel) and right (right panel) sides of the upper and lower edges.

The top and bottom panels of the graphs refer to the top and bottom edges of the tower walls, respectively. As in the previous figure, data from each side of the tower were grouped by segments. The analysis showed a trend in the TLS and UAV differences values between the parameters. The highest values for the bottom edge (bottom panel of **Fig. 16**) occurred for the lowest tower segment #1, and for the top edge (top panel of **Fig. 16**) for the highest segment #4.

The linear deviations of the axis position dM^{i}_{PCSE} (left panel of **Fig. 16**) are expressed relative to the theoretical position of the walls defined by the geometry of the octagonal cross-section of the tower (cf. **Section 2.3.3**). The mean values of the deviations at the lower edge ($dM^{i,bot}_{PCSE}$) did not exceed 0.01 m (segments #2 - #4) except for one case of 0.02 m (segment #1). The standard deviations of the deviations were about 70% of the mean values. The upper edge obtained the largest values of the deviations $dM^{i,top}_{PCSE}$ for the highest segment #4 (0.016 m ± 0.005 m). The lower segments (#1 - #3) obtained average values not exceeding 0.1 m, and standard deviations not exceeding 0.005 m. The angular parameter δ^{i}_{PCSE} derived from the linear deviations dM^{i}_{PCSE} takes into account the decreasing distance of successive horizontal edges from the axis of symmetry of the tower with the height of the tower. The previously observed trend repeated. The average values of the angle deviations on the lower edge of segment #1 ($\delta^{1,bot}_{PCSE}$) and on the upper edge of segment #4 ($\delta^{4,\ top}_{PCSE}$) in both cases took the highest value of 0.15°. However, the standard deviation of the lower edge was twice as large as of the upper edge. The values of the deviations δ^{i}_{PCSE} in the remaining segments did not exceed 0.06° in average values.

The deviations of the PCSE depth parameter expressed separately for the left ($dz^{i,left}_{PCSE}$) and right ($dz^{i,right}_{PCSE}$) edges at the top (*top*) and bottom (*bot*) of each of the eight walls took similar values. The highest mean values occurred for the lower edge of segment #1 (about 0.020 m) and the upper edge of segment #4 (about 0.013 m). The above extreme values were also characterized by the values of standard deviations several times larger than in the case of the other segments (cf. the middle and right panels of **Fig. 16**). The smallest deviations of the dz^{i}_{PCSE} parameter were observed in the two middle segments (#2 and #3).

The integration of TLS and UAV point clouds was carried out using a six-parameter Helmert transformation (the scale factor was eliminated by using a linear unit from the SI system in both LIDAR sensors). The rotation angles and translation vector coordinates were determined based on the results of multi-module symmetry axis estimation procedures, point cloud verticalization, and cardinal orientation. As a result of the transformation, the TLS and ALS point clouds of the Gediminas Tower in Vilnius are shifted to the origin of the coordinate system while maintaining the geographic orientation of the object's walls. The resulting local coordinate system satisfies the harmonization condition.

The process of determining the transformation parameters of two datasets in both cases proceeds similarly, based on the analysis of the plane profiles of the tower's walls. The difference in data processing arises from the differences in the technology used for terrestrial and airborne surveys. The TLS point cloud usually has a higher resolution than the ALS point cloud, with the latter providing greater surface coverage of the object. This is especially useful for roofs that are inaccessible for terrestrial measurements. The varying resolution of the TLS and ALS point clouds, as well as the irregular distribution of points on the object's surface, must be taken into account in the Hausdorff distance analyses used in Cloud-to-Cloud comparisons **[77]**. This issue is addressed through the analysis of the discrete surface profile of the object, determined in the process of local plane fitting using the least squares method (**Fig. 17**).

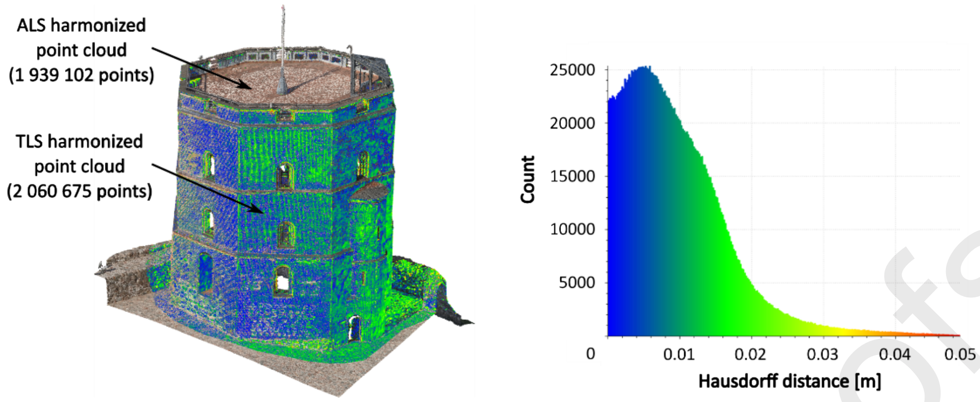

Fig. 17. Comparison of integrated TLS and ALS point clouds.

The harmonization (integration) of the TLS and ALS point clouds of the Gediminas Tower achieved an average error of 8 mm. The TLS point cloud was subsampled for the analysis to obtain a number of points similar to that of the ALS point cloud. Due to the different point density distributions in the clouds and the varying extent of surface coverage of the tower, the analysis was limited to a threshold value of 5 cm. This approach is justified, as the remaining points, such as those located on the tower's roof in the ALS point cloud in **Fig. 17**, do not have counterparts in the compared TLS cloud and would result in Hausdorff distance values significantly exceeding the set threshold value.

4 Conclusions

The paper proposes a new input of geometrical parameters to the HBIM datasets regarding the issue of symmetry of historical buildings. Symmetry is one of the principal features of historical structures, eg. medieval towers. The current state-of-the-art of the HBIM doesn't cover this topic in detail, hence the aim of the study was to present a uniform methodology to quantify the factor of symmetry of historical structures on the example of the Gediminas Tower in Vilnius. Three new HBIM symmetry features describe the object's multi-modal axis, the topology of regularly distributed wall panels, and the configuration of vertical edges of the object's walls. The proposed approach utilizes the prismatic variant of the PCSE method to obtain the processed dataset describing the relation of the point cloud with the estimated object's axis of symmetry. Along with the new HBIM symmetry parameters, the paper describes significant improvements to the PCSE algorithm itself by introducing a new approach to the segmentation of point clouds according to the geographical cardinal directions of the tower walls.

The second aspect of the study involved the application of LiDAR TLS and UAV measurements which are currently the most reliable and efficient methods of creating a digital twin of historical buildings. Taking into account the limitations of both LiDAR methods, the study aims to compare TLS and UAV point clouds by determining the HBIM symmetry parameters individually for each dataset. The case of the Gediminas Tower showed high convergence of the TLS- and UAV-derived results and confirmed the validity of using both methods in assessing the geometry of historical symmetrical buildings. Differences in linear HBIM parameters, took mean values of single centimeters, with some cases below one centimeter. Differences in angular HBIM parameters most often did not exceed 1° with exceptions concerning the horizontal orientation of the estimated axis and the direction of the slope of the tower walls. The detected pattern of major asymmetries in the lower horizontal edge of the lowest segment (#1) and the upper edge of the highest segment (#4) indicates the sensitivity of both LiDAR measurement methods to the irregularity, point cloud occlusions, and height of the wall panels' structure.

Summing up, the study showed obtaining similar values of the HBIM symmetry parameters from the TLS and UAV point clouds of the Tower of Gediminas, which means that both LiDAR technologies provide valid and precise information on the symmetry of historical buildings. The factor of the universality of the proposed methodology enables its adaptation to other symmetrical objects. A uniform approach to defining the geometry of historical buildings is an argument to include the introduced symmetry features in the HBIM datasets.

Acknowledgements

Thanks to the National Museum of Lithuania for allowing the measurements of the Tower of the Gediminas.

Thanks to Mr Kazys Pleskis from Vilnius University of Technology for carrying out the GNSS measurements to determine the coordinates of the ground control points.

Support of these studies from Gdansk University of Technology by the DEC-26/2021/IDUB/I.3.3 and 11/1/2023/IDUB/I3b/A grants under the Argentum Triggering Research Grants, and the 1/1/2023/IDUB/II.2b/Np grant under the Neptunium Enhancing Baltic Region Research Cooperation, 'Excellence Initiative—Research University' programs is gratefully acknowledged.

References

[1] Murphy, M., McGovern, E., & Pavia, S. (2009). Historic building information modelling (HBIM). Structural Survey, 27(4), 311-327, doi: 10.1108/02630800910985108.
[2] Murphy, M., McGovern, E., & Pavia, S. (2013). Historic Building Information Modelling–Adding intelligence to laser and image based surveys of European classical architecture. ISPRS journal of photogrammetry and remote sensing, 76, 89-102, doi: 10.1016/j.isprsjprs.2012.11.006.
[3] Arayici, Y., Counsell, J., Mahdjoubi, L., Nagy, G., Ḥawwās, S. Z., & Dweidar, K. (Eds.). (2017). Heritage building information modelling. Abingdon: Routledge, Taylor and Francis Group, London and New York., ISBN: 978-1-138-64568-4.
[4] Jordan-Palomar, I., Tzortzopoulos, P., García-Valldecabres, J., & Pellicer, E. (2018). Protocol to manage heritage-building interventions using heritage building information modelling (HBIM). Sustainability, 10(4), 908, doi: 10.3390/su10040908.
[5] Martinelli, L., Calcerano, F., & Gigliarelli, E. (2022). Methodology for an HBIM workflow focused on the representation of construction systems of built heritage. Journal of Cultural Heritage, 55, 277-289, doi: doi: 10.1016/j.culher.2022.03.016.
[6] Korumaz, S. A. G., & Sayar, R. (2022). Deviation Analysis of Historical Building Based on Terrestrial Laser Scanner Data and 3D Mesh Model. Advanced LiDAR, 2(1), 21-30.
[7] Carvajal-Ramírez, F., Martínez-Carridondo, P., Yero-Paneque, L., & Agüera-Vega, F. (2019). UAV Photogrammetry and HBIM for the Virtual Reconstruction of Heritage. The International Archives of the Photogrammetry, Remote Sensing and Spatial Information Sciences, 42, 271-278, doi: 10.5194/isprs-archives-XLII-2-W15-271-2019.
[8] Martínez-Carricondo, P., Carvajal-Ramírez, F., Yero-Paneque, L., & Agüera-Vega, F. (2021). Combination of HBIM and UAV photogrammetry for modelling and documentation of forgotten heritage. Case study: Isabel II dam in Níjar (Almería, Spain). Heritage Science, 9(1), 95, doi: 10.1186/s40494-021-00571-8.
[9] Candan, L., & Kaçar, E. (2023). Methodology of real-time 3D point cloud mapping with UAV lidar. International Journal of Engineering and Geosciences, 8(3), 301-309, doi: 10.26833/ijeg.1178260.
[10] Yakar, M., & Yılmaz, H. M. (2010). Comparative evaluation of excavation volume by TLS and total topographic station based methods. Lasers in Engineering, 19, 331–345.
[11] Sevgen, S. C., & Karsli, F. (2020). Automatic ground extraction for urban areas from airborne lidar data. Turkish Journal of Engineering, 4(3), 113-122, doi: 10.31127/tuje.641501.
[12] Özdemir, S., Akbulut, Z., Karslı, F., & Acar, H. (2021). Automatic extraction of trees by using multiple return properties of the lidar point cloud. International Journal of Engineering and Geosciences, 6(1), 20-26, doi: 10.26833/ijeg.668352.
[13] Cotella, V. A. (2023). From 3D point clouds to HBIM: application of artificial intelligence in cultural heritage. Automation in Construction, 152, 104936, doi: 10.1016/j.autcon.2023.104936.
[14] Moyano, J., Musicco, A., Nieto-Julián, J. E., & Domínguez-Morales, J. P. (2024). Geometric characterization and segmentation of historic buildings using classification algorithms and convolutional networks in HBIM. Automation in Construction, 167, 105728, doi: 10.1016/j.autcon.2024.105728.
[15] Khodeir, L. M., Aly, D., & Tarek, S. (2016). Integrating HBIM (Heritage Building Information Modeling) tools in the application of sustainable retrofitting of heritage buildings in Egypt. Procedia Environmental Sciences, 34, 258-270, doi: 10.1016/j.proenv.2016.04.024.
[16] International Organization for Standardization. (2024). Industry Foundation Classes (IFC) for data sharing in the construction and facility management industries. Part 1: Data schema (ISO Standard No. 16739-1:2024). Retrieved from https://www.iso.org/standard/84123.html
[17] International Organization for Standardization. (2018). Organization and digitization of information about buildings and civil engineering works, including building information modelling (BIM) — Information management using building information modelling. Part 2: Delivery phase of the assets (ISO Standard No. 19650-2:2018). Retrieved from https://www.iso.org/standard/68080.html
[18] Chelaru, B., Onuțu, C., Ungureanu, G., & Șerbănoiu, A. A. (2024). Integration of point cloud, historical records, and condition assessment data in HBIM. Automation in Construction, 161, 105347, doi: 10.1016/j.autcon.2024.105347.
[19] Penjor, T., Banihashemi, S., Hajirasouli, A., & Golzad, H. (2024). Heritage building information modeling (HBIM) for heritage conservation: Framework of challenges, gaps, and existing limitations of HBIM. Digital Applications in Archaeology and Cultural Heritage, 35, e00366, doi: 10.1016/j.daach.2024.e00366.
[20] Barazzetti, L., Banfi, F., Brumana, R., Gusmeroli, G., Previtali, M., & Schiantarelli, G. (2015). Cloud-to-BIM-to-FEM: Structural simulation with accurate historic BIM from laser scans. Simulation modelling practice and theory, 57, 71-87, doi: 10.1016/j.simpat.2015.06.004.

[21] Quattrini, R., Malinverni, E. S., Clini, P., Nespeca, R., & Orlietti, E. (2015). From TLS to HBIM. High quality semantically-aware 3D modeling of complex architecture. The International Archives of the Photogrammetry, Remote Sensing and Spatial Information Sciences, 40, 367-374, doi: 10.5194/isprsarchives-XL-5-W4-367-2015.
[22] Dore, C., & Murphy, M. (2013). Semi-automatic modelling of building facades with shape grammars using historic building information modelling. The International Archives of the Photogrammetry, Remote Sensing and Spatial Information Sciences, 40, 57-64, doi: 10.5194/isprsarchives-XL-5-W1-57-2013.
[23] Fai, S., Rafeiro, J., 2014. Establishing an Appropriate Level of Detail (LoD) for a Building Information Model (BIM)-West Block, Parliament Hill, Ottawa, Canada. ISPRS Annals of Photogrammetry, Remote Sensing and Spatial Information Sciences, 1, 123-130, doi: 10.5194/isprsannals-II-5-123-2014.
[24] Bruno, S., De Fino, M., & Fatiguso, F. (2018). Historic Building Information Modelling: performance assessment for diagnosis-aided information modelling and management. Automation in Construction, 86, 256-276, doi: 10.1016/j.autcon.2017.11.009.
[25] Martinelli, L., Calcerano, F., & Gigliarelli, E. (2022). Methodology for an HBIM workflow focused on the representation of construction systems of built heritage. Journal of Cultural Heritage, 55, 277-289, doi: 10.1016/j.culher.2022.03.016.
[26] Brumana, R., Oreni, D., Raimondi, A., Georgopoulos, A., & Bregianni, A. (2013, October). From survey to HBIM for documentation, dissemination and management of built heritage: The case study of St. Maria in Scaria d'Intelvi. In 2013 Digital Heritage International Congress (DigitalHeritage) (Vol. 1, pp. 497-504). IEEE, doi: 10.1109/DigitalHeritage.2013.6743789.
[27] Attico, D., Turrina, A., Banfi, F., Grimoldi, A., Landi, A., Condoleo, P., & Brumana, R. (2019). The HBIM analysis of the geometry to understand the constructive technique: the use of the trompe volume in a brick vault. The International Archives of the Photogrammetry, Remote Sensing and Spatial Information Sciences, 42, 107-114, doi: 10.5194/isprs-archives-XLII-2-W11-107-2019.
[28] Liu, J., Azhar, S., Willkens, D., & Li, B. (2023, April). Static terrestrial laser scanning (TLS) for heritage building information modeling (HBIM): a systematic review. In Virtual Worlds (Vol. 2, No. 2, pp. 90-114). MDPI, doi: 10.3390/virtualworlds2020006.
[29] da Silva Ruiz, P. R., Almeida, C. M. D., Schimalski, M. B., Liesenberg, V., & Mitishita, E. A. (2023). Multi-approach integration of ALS and TLS point clouds for a 3-D building modeling at LoD3. International Journal of Architectural Computing, 21(4), 652-678, doi: 10.1177/1478077123117602.
[30] Castorena, J., Dickman, L. T., Killebrew, A. J., Gattiker, J. R., Linn, R., & Loudermilk, E. L. (2023). Automated structural-level alignment of multi-view TLS and ALS point clouds in forestry. arXiv preprint arXiv:2302.12989, doi: 10.48550/arXiv.2302.12989.
[31] Costa, A. P., Cuperschmid, A. R. M., & Neves, L. O. (2024). HBIM and BEM association: Systematic literature review. Journal of Cultural Heritage, 66, 551-561, doi: 10.1016/j.culher.2024.01.008.
[32] Rolim, R., López-González, C., & Viñals, M. J. (2024). Analysis of the Current Status of Sensors and HBIM Integration: A Review Based on Bibliometric Analysis. Heritage, 7(4), 2071-2087, doi: 10.3390/heritage7040098.
[33] Liu, J., & Li, B. (2024). Heritage Building Information Modelling (HBIM): A Review of Published Case Studies. The International Archives of the Photogrammetry, Remote Sensing and Spatial Information Sciences, 48, 387-393, doi: 10.5194/isprs-archives-XLVIII-1-2024-387-2024.
[34] López, F. J., Lerones, P. M., Llamas, J., Gómez-García-Bermejo, J., & Zalama, E. (2018). A review of heritage building information modeling (H-BIM). Multimodal Technologies and Interaction, 2(2), 21, doi: 10.3390/mti2020021.
[35] Del Rio, I., Cabaleiro, M., Conde, B., Riveiro, B., Caamaño, J. C., & El Naggar, H. (2020). Hbim application to historical steel structures: The case study of lapela bridge. In 5th World Congress on Civil, Structural and Environmental Engineering (p. 160). ICSECT, doi: 10.11159/icsect20.160.
[36] Cappuccino, F., Flenghi, G., & Russo, M. (2024, March). 3D Acquisition and HBIM Modeling of Medieval Architectures in Rome: The Albergo of the Catena. In Congreso Internacional de Expresión Gráfica Arquitectónica (pp. 57-64). Cham: Springer Nature Switzerland, doi: 10.1007/978-3-031-57583-9_8.
[37] Hargittai, I., & Hargittai, M. (2015). The universality of the symmetry concept. Architecture and Mathematics from Antiquity to the Future: Volume I: Antiquity to the 1500s, 603-618, doi: 10.1007/978-3-319-00137-1_40.
[38] Mehaffy, M. W. (2020). The Impacts of symmetry in architecture and urbanism: Toward a new research agenda. Buildings, 10(12), 249, doi: 10.3390/buildings10120249.
[39] Hubert, H. W. (2021). Symmetry and Symmetry: The Notion of the Antique Term Symmetria before its New Definition in the Renaissance. European Review, 29(2), 210-225, doi: 10.1017/S1062798720000381.
[40] López González, M. C., & García-Valldecabres, J. (2018, May). Parametric processes in implementing H-BIM on historical architecture. In Congreso Internacional de Expresión Gráfica Arquitectónica (pp. 940-950). Cham: Springer International Publishing, doi: 10.1007/978-3-319-93749-6_76.
[41] Bianchini, C., & Potestà, G. (2021). BIM for built cultural heritage: semantic segmentation, architectural stratification and LOD of the baptistery of San Giovanni in Florence. In From Building Information Modelling to Mixed Reality (pp. 1-15). Springer International Publishing, doi: 10.1007/978-3-030-49278-6_1.
[42] Martinelli, L., Calcerano, F., & Gigliarelli, E. (2022). Methodology for an HBIM workflow focused on the representation of construction systems of built heritage. Journal of Cultural Heritage, 55, 277-289, doi: 10.1016/j.culher.2022.03.016.
[43] Dąbrowski, P.S. (2024). Przestrzenne rozwinięcia chmur punktów. Podstawy teoretyczne oraz przykłady aplikacyjne. Wydawnictwo Politechniki Gdańskiej, Gdańsk, Poland, ISBN 978-83-7348-909-7 (in Polish).
[44] Dabrowski. P. S., & Specht. C. (2019). Spatial expansion of the symmetrical objects point clouds to the lateral surface of the cylinder–Mathematical model. Measurement. 134. 40-47, doi: 10.1016/j.measurement.2018.10.036.
[45] Dabrowski. P. S., Zienkiewicz. M. H., Truong-Hong. L., & Lindenbergh. R. (2023). Assessing historical church tower asymmetry using point cloud spatial expansion. Journal of Building Engineering. 75. 107040, doi: 10.1016/j.jobe.2023.107040.

[46] Milkulėnas, V., Minkevičius, V., & Satkūnas, J. (2017). Gediminas's Castle Hill (in Vilnius) case: Slopes failure through historical times until present. In Advancing Culture of Living with Landslides: Volume 5 Landslides in Different Environments (pp. 69-76). Springer International Publishing, doi: 10.1007/978-3-319-53483-1_10.
[47] Skuodis, Š., Daugevičius, M., Medzvieckas, J., Šneideris, A., Jokūbaitis, A., Rastenis, J., & Valivonis, J. (2023, October). Remains of Gediminas Castle Hill (Vilnius, Lithuania): 3D Numerical Model Behaviour. In International Conference Modern Building Materials, Structures and Techniques (pp. 3-16). Cham: Springer Nature Switzerland, doi: 10.1007/978-3-031-44603-0_1.
[48] Skuodis, Š., Daugevičius, M., Medzvieckas, J., Šneideris, A., Jokūbaitis, A., Rastenis, J., & Valivonis, J. (2022). Gediminas Hill slopes behavior in 3D finite element model. Buildings, 12(8), 1113, doi: 10.3390/buildings12081113.
[49] Girardeau-Montaut, D. (2016). CloudCompare. France: EDF R&D Telecom ParisTech, 11(5), 2016.
[50] Rusinkiewicz, S., & Levoy, M. (2001, May). Efficient variants of the ICP algorithm. In Proceedings third international conference on 3-D digital imaging and modeling (pp. 145-152). IEEE, doi: 10.1109/IM.2001.924423.
[51] Tysiac, P., Sieńska, A., Tarnowska, M., Kedziorski, P., & Jagoda, M. (2023). Combination of terrestrial laser scanning and UAV photogrammetry for 3D modelling and degradation assessment of heritage building based on a lighting analysis: case study—St. Adalbert Church in Gdansk, Poland. Heritage Science, 11(1), 53, doi: 10.1186/s40494-023-00897-5.
[52] Xu, N., Qin, R., & Song, S. (2023). Point cloud registration for LiDAR and photogrammetric data: A critical synthesis and performance analysis on classic and deep learning algorithms. ISPRS open journal of photogrammetry and remote sensing, 8, 100032, doi: 10.1016/j.ophoto.2023.100032.
[53] Sanz-Ablanedo, E., Chandler, J. H., Rodríguez-Pérez, J. R., & Ordóñez, C. (2018). Accuracy of unmanned aerial vehicle (UAV) and SfM photogrammetry survey as a function of the number and location of ground control points used. Remote Sensing, 10(10), 1606, doi: 10.3390/rs10101606.
[54] Rousseeuw. P. J., & Hubert. M. (2011). Robust statistics for outlier detection. Wiley interdisciplinary reviews: Data mining and knowledge discovery. 1(1). 73-79, doi: 10.1002/widm.2.
[55] Giannetti, F., Puletti, N., Quatrini, V., Travaglini, D., Bottalico, F., Corona, P., & Chirici, G. (2018). Integrating terrestrial and airborne laser scanning for the assessment of single-tree attributes in Mediterranean forest stands. European Journal of Remote Sensing, 51(1), 795-807, doi: 10.1080/22797254.2018.1482733.
[56] Teng, J., Shi, Y., Wang, H., & Wu, J. (2022). Review on the research and applications of TLS in ground surface and constructions deformation monitoring. Sensors, 22(23), 9179, doi: 10.3390/s22239179.
[57] Wang, L., Chen, H., & You, Z. (2024). Combining geometrical and intensity information to recognize vehicles from super-high density UAV-LiDAR point clouds. Scientific Reports, 14(1), 25097, doi: 10.1038/s41598-024-75968-z.
[58] Nap, M. E., Chiorean, S., Cira, C. I., Manso-Callejo, M. Á., Păunescu, V., Șuba, E. E., & Sălăgean, T. (2023). Non-destructive measurements for 3D modeling and monitoring of large buildings using terrestrial laser scanning and unmanned aerial systems. Sensors, 23(12), 5678, doi: 10.3390/s23125678.
[59] Choi, S. K., Ramirez, R. A., & Kwon, T. H. (2023). Acquisition of high-resolution topographic information in forest environments using integrated UAV-LiDAR system: System development and field demonstration. Heliyon, 9(9), doi: 10.1016/j.heliyon.2023.e20225.
[60] Frachetti, M. D., Berner, J., Liu, X., Henry, E. R., Maksudov, F., & Ju, T. (2024). Large-scale medieval urbanism traced by UAV–lidar in highland Central Asia. Nature, 1-7, doi: 10.1038/s41586-024-08086-5.
[61] Lenda, G., Borowiec, N., & Marmol, U. (2023). Study of the Precise Determination of Pipeline Geometries Using UAV Scanning Compared to Terrestrial Scanning, Aerial Scanning and UAV Photogrammetry. Sensors, 23(19), 8257, doi: 10.3390/s23198257.
[62] Wang, Z., Zhang, Y., Li, F., Gao, W., Guo, F., Li, Z., & Yang, Z. (2024). Regional mangrove vegetation carbon stocks predicted integrating UAV-LiDAR and satellite data. Journal of Environmental Management, 368, 122101, doi: 10.1016/j.jenvman.2024.122101.
[63] Besl, P. J., & McKay, N. D. (1992, April). Method for registration of 3-D shapes. In Sensor fusion IV: control paradigms and data structures (Vol. 1611, pp. 586-606). Spie.
[64] Zhang, Z. (1994). Iterative point matching for registration of free-form curves and surfaces. International journal of computer vision, 13(2), 119-152.
[65] Chen, Y., & Medioni, G. (1992). Object modelling by registration of multiple range images. Image and vision computing, 10(3), 145-155, doi: 10.1016/0262-8856(92)90066-C.
[66] Schütz, M., Ohrhallinger, S., & Wimmer, M. (2020, October). Fast out-of-core octree generation for massive point clouds. In Computer Graphics Forum (Vol. 39, No. 7, pp. 155-167), doi: 10.1111/cgf.14134.
[67] Elseberg, J., Borrmann, D., & Nüchter, A. (2013). One billion points in the cloud–an octree for efficient processing of 3D laser scans. ISPRS Journal of Photogrammetry and Remote Sensing, 76, 76-88, doi: 10.1016/j.isprsjprs.2012.10.004.
[68] Fischler. M. A., & Bolles. R. C. (1981). Random sample consensus: a paradigm for model fitting with applications to image analysis and automated cartography. Communications of the ACM. 24(6). 381-395, doi: 10.1145/358669.358692.
[69] Dabrowski, P. S., & Zienkiewicz, M. H. (2022). Impact of cross-section centers estimation on the accuracy of the point cloud spatial expansion using robust M-estimation and Monte Carlo simulation. Measurement, 189, 110436, doi: 10.1016/j.measurement.2021.110436.
[70] Snow. K., & Schaffrin. B. (2016). Line fitting in Euclidean 3D space. Studia geophysica et geodaetica. 60. 210-227, doi: 10.1007/s11200-015-0246-x.
[71] Roman. S., Axler. S., & Gehring. F. W. (2005). Advanced linear algebra (Vol. 3). New York: Springer, ISBN 0-387-24766-1.
[72] Dabrowski. P. S. (2022). Novel PCSE-based approach of inclined structures geometry analysis on the example of the Leaning Tower of Pisa. Measurement. 189. 110462, doi: 10.1016/j.measurement.2021.110462.
[73] Staudte. R. G., & Sheather. S. J. (2011). Robust estimation and testing. John Wiley & Sons, ISBN 0-471-85547-2.

[74] NIMA (2004). NIMA TR 8350.2. Department of Defense World Geodetic System 1984: Its Definition and Relationships with Local Geodetic Systems. Third Edition. National Imagery and Mapping Agency. 3 January 2004, Retrieved from https://earth-info.nga.mil/php/download.php?file=coord-wgs84.
[75] Li, L., Wang, R., & Zhang, X. (2021). A tutorial review on point cloud registrations: principle, classification, comparison, and technology challenges. Mathematical Problems in Engineering, 2021(1), 9953910, doi: 10.1155/2021/9953910.
[76] Han. X. F., Jin. J. S., Wang. M. J., Jiang. W., Gao. L., & Xiao. L. (2017). A review of algorithms for filtering the 3D point cloud. Signal Processing: Image Communication. 57. 103-112, doi: 10.1016/j.image.2017.05.009.
[77] Huttenlocher, D. P., Klanderman, G. A., & Rucklidge, W. J. (1993). Comparing images using the Hausdorff distance. IEEE Transactions on pattern analysis and machine intelligence, 15(9), 850-863, doi: 10.1109/34.232073.

Extension of HBIM datasets by the factor of geometrical symmetry
A unified approach applicable to various symmetrical structures
Validation of the methodology using TLS and UAV LiDAR point clouds
Assessment of applicability of TLS and UAV LiDAR in HBIM parametrization

Acknowledgements

Thanks to the National Museum of Lithuania for allowing the measurements of the Tower of the Gediminas.

Thanks to Mr Kazys Pleskis from Vilnius University of Technology for carrying out the GNSS measurements to determine the coordinates of the ground control points.

Support of these studies from Gdansk University of Technology by the DEC-26/2021/IDUB/I.3.3 and 11/1/2023/IDUB/I3b/A grants under the Argentum Triggering Research Grants, and the 1/1/2023/IDUB/II.2b/Np grant under the Neptunium Enhancing Baltic Region Research Cooperation, 'Excellence Initiative—Research University' programs is gratefully acknowledged.

Declaration of interests

☒ The authors declare that they have no known competing financial interests or personal relationships that could have appeared to influence the work reported in this paper.

☐ The authors declare the following financial interests/personal relationships which may be considered as potential competing interests: